

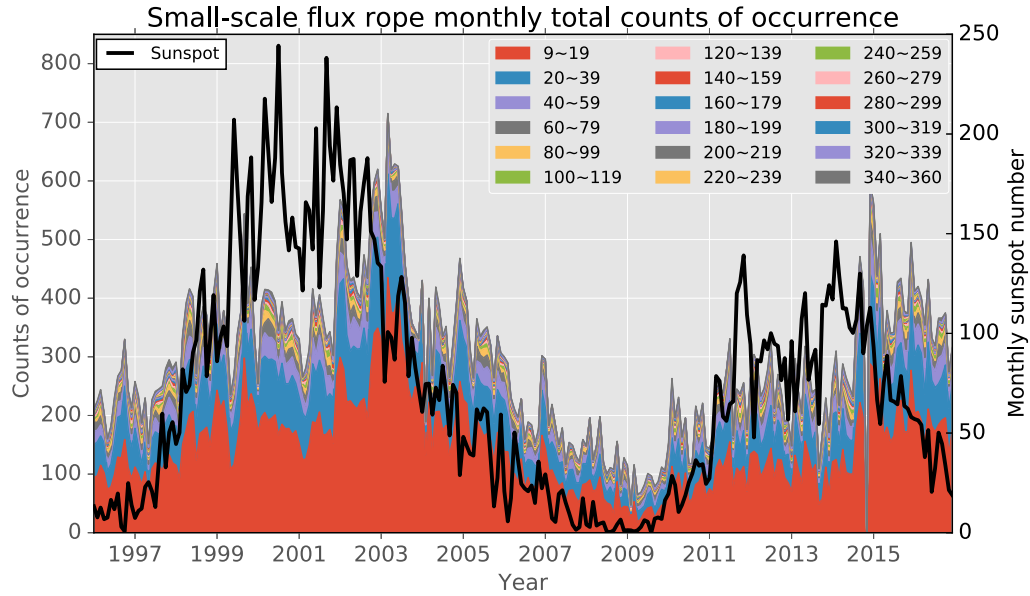
## CHAPTER 4

### SMALL-SCALE MAGNETIC FLUX ROPE DATABASE AND STATISTICAL ANALYSIS

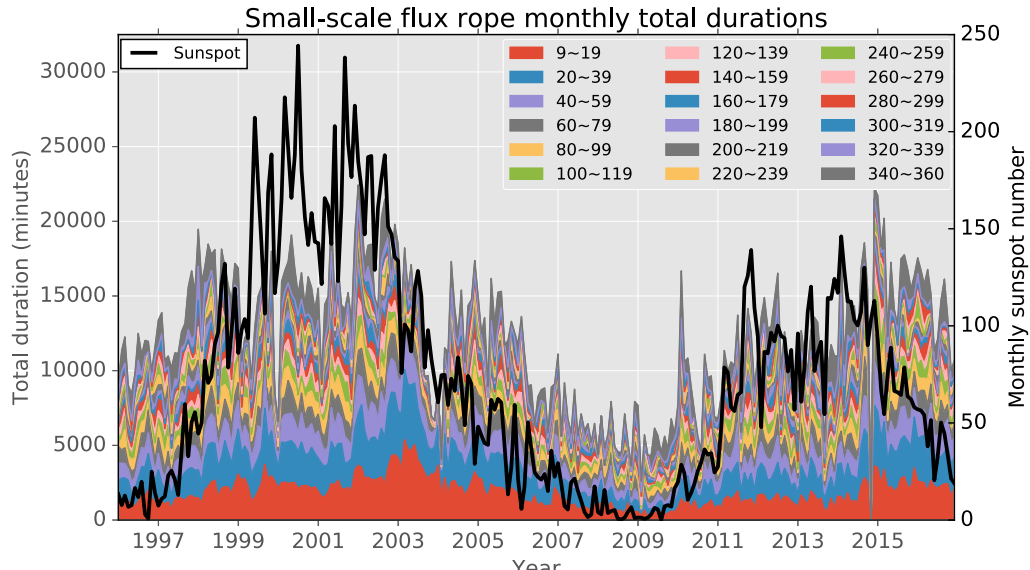
We have applied the automated detection algorithm described in Chapter 3 to magnetic field and plasma data from the Wind spacecraft, and published the database online (<http://fluxrope.info>). A brief overview of the database was given in section 3.3. In this chapter, we will discuss the properties of the detected small-scale magnetic flux ropes derived from the statistical analysis results based on the database.

#### 4.1 Occurrence Rate of Small-scale Magnetic Flux Ropes

As discussed in Chapter 1, there is a long-standing debate on the origin of small-scale magnetic flux ropes. Since the Sun is the dominant source in the heliosphere, the occurrence rate of most plasma dynamic processes is more or less dependent on the solar activity cycle, either positively or negatively. Although the occurrence rate dependency does not directly answer the question on the origin of small-scale magnetic flux ropes, we can still get valuable clues by comparing its dependency to that of other plasma processes or structures, such as some other solar eruptive processes, especially magnetic clouds.



(a)



(b)

**Figure 4.1:** (a) The monthly counts of flux rope events occurrence (left axis) and the monthly sunspot number (black curve; right axis) during 1996-2016. Colors represent counts of events with different durations as indicated by the legend in minutes. (b) The monthly flux rope total duration (left axis) and the monthly sunspot number (right axis) during 1996-2016. The format is the same as in (a).

Figure 4.1 (a) shows the monthly occurrence counts of small-scale flux ropes from 1996 to 2016, covering solar cycles 23 (from May 1996 to January 2008), and 24, which began in December 2008, reached its maximum in April 2014, and may have ended in early 2017. The different colors represent different durations of small-scale flux ropes (from 9 minutes to 360 minutes), and the thick black curve is the corresponding monthly sunspot number. The events of smaller durations generally have greater rates of occurrence. Clearly the total counts including all events of variable durations follow the monthly sunspot numbers, hinting at solar-cycle dependency of these events. Note that the occurrence counts also vary cycle by cycle. From the sunspot numbers we can see that the solar activity in cycle 23 is more intense than that of cycle 24, and accordingly, the overall small-scale flux rope occurrence counts in cycle 23 is larger than those of cycle 24, approximately proportional to sunspot numbers. The peaks of occurrence counts tend to appear in the declining phase of each solar cycle.

Figure 4.1 (b) is the monthly total durations of small-scale flux ropes from 1996 to 2016. The format is the same as Figure 4.1 (a). In Figure 4.1 (b), the  $y$ -axis represents the total small-scale flux rope duration in each month. Although in the monthly duration plot, the area taken up by smaller flux ropes is suppressed, the solar cycle dependency shown in Figure 4.1 (a) still persists in Figure 4.1 (b). This plot shows that the solar cycle dependency is not only attributed to smaller flux ropes, but also to relatively larger flux ropes.

Cartwright and Moldwin [72] carried out an earlier study of identifying and characterizing small-scale flux ropes in the solar wind with durations  $\geq 10$  minutes,

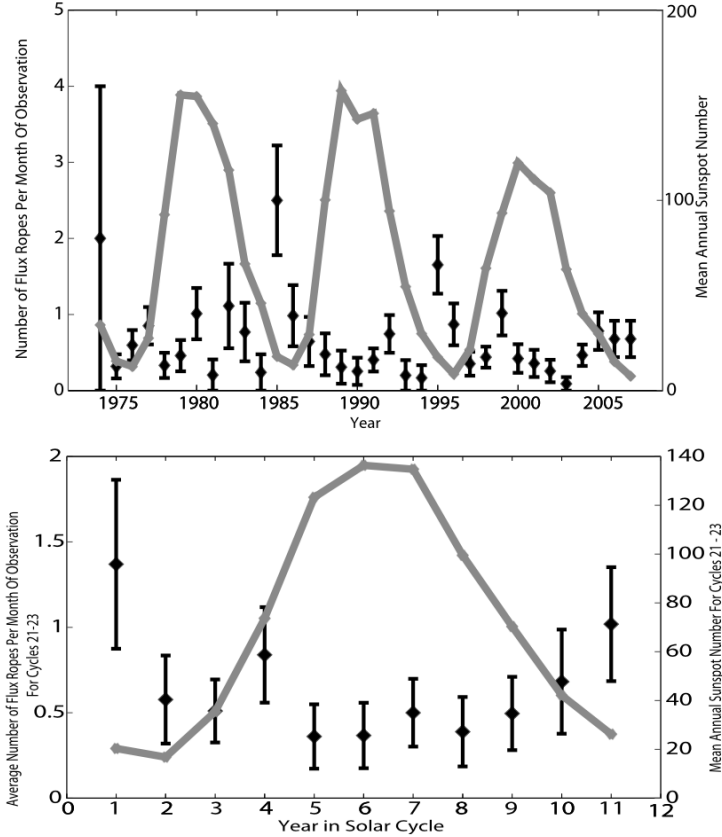


**Figure 4.2:** The upper panel is small-scale flux rope occurrence counts per month of observation for  $1974 \sim 2006$ . The lower panel is the monthly occurrence counts averaged over solar cycles 21 to 23. Gray curves show the corresponding sunspot numbers. (Credit: Cartwright and Moldwin [72]).

similar to the range of durations we examined. They surveyed small-scale flux ropes between heliocentric distance 0.3 and 5.5 AU, from 1974 to 2007. They found that the occurrence rate of small-scale magnetic flux ropes has a negative solar cycle dependency. More events tend to occur during solar minimum rather than solar maximum. From the lower panel of Figure 4.2, one can see that the averaged monthly occurrence counts of small-scale flux ropes have a negative correlation with the averaged annual sunspot number, in contrast to the result from our database shown in Figure 4.1 (a).

Taking a closer look at the upper panel of Figure 4.2, we find that the solar cycle dependency varies cycle by cycle. In solar cycle 21 (1976  $\sim$  1986), the small-scale flux rope occurrence seems to be positively correlated with sunspot numbers. However, the correlation seems to be negative in solar cycle 22 (1986  $\sim$  1996). In solar cycle 23 (1996 $\sim$ 2008; the plot only covers 1996 to 2007), the occurrence trend seems to follow sunspot numbers from 1997 to 2003, but has no clear trend from 2004 to 2007. However, in Figure 4.1 (a), the trend of occurrence rate shows consistency with the sunspot numbers in solar cycle 23. Cartwright and Moldwin's database included small-scale flux ropes from 0.3 to 5 AU. Our database only includes the ones at 1 AU. This may be one of the reasons leading to the difference in this statistical result. The other reason is that the total number of events in Cartwright and Moldwin's database is far too few,  $\sim$  1 per month, on average, as apposed to  $\sim$  hundreds per month in our database.

Figure 4.2 shows that the small-scale flux ropes occur more frequently during solar minimum than during solar maximum. If we believe that the small-scale flux ropes have the same origin as magnetic clouds, they should have the similar solar cycle dependency. Since magnetic clouds occur more frequently during solar maximum than in solar minimum, one would expect more small-scale flux ropes during solar maximum. However, Figure 4.2 indicates the opposite situation, which was used by those authors as evidence to refute the hypothesis that the small-scale flux ropes come from the Sun.

Feng et al. [69, 71] investigated the small to intermediate size magnetic flux ropes that had durations mostly beyond the range we examined. They suggested

that the small-scale flux ropes are interplanetary manifestations of small CMEs, originating from weak solar eruptions and forming in the solar corona, just like magnetic clouds. Feng et al. [71] found a positive correlation between the occurrence rate of small- and intermediate-scale magnetic flux ropes and the occurrence rate of magnetic clouds from 1995 to 2005. Therefore, they called these small- and intermediate-scale magnetic flux ropes as small magnetic clouds (SMCs). However, the occurrence trend of SMCs shown by Feng et al. [71] (Figure 4 in their paper) is not consistent with the trend of sunspot numbers, which is also different from what is shown in Figure 4.1 (a). As pointed out by Cartwright et al. [72], Feng et al. [71] did not exclude Alfvén waves in their database. Another caveat weakening their conclusion is that the total number of events in their database is also very small.

Gopalswamy et al. [131] investigated the correlation between the annual number of magnetic cloud events and the frontside halo CMEs, and compared both with the sunspot numbers. One can see from Figure 4.3 that the main trend of magnetic cloud occurrence counts is consistent with the trend of sunspot numbers. It is because the magnetic clouds originate from the Sun, as is widely accepted. When comparing Figure 4.3 with Figure 4.1 (a), one can see that the small-scale flux rope occurrence rate in Figure 4.1 (a) changes in a way consistent with the change of magnetic cloud occurrence rate in Figure 4.3. During solar maximum, there are more magnetic clouds and small-scale flux ropes occurring, and there are fewer during solar minimum. If both magnetic clouds and small-scale flux ropes originate from solar eruptions, they may share the same dependency with solar activity. However, this fact is still not a sufficient condition indicating that the small-scale flux ropes originate from the

Sun. On one hand, there may be two populations of small-scale flux ropes which have different origins and different solar cycle dependencies, i.e., one population has solar cycle dependency but the other does not. When they are mixed, the solar cycle dependency may still appear. On the other hand, even if all small-scale flux rope events have solar cycle dependency as magnetic clouds do, we still cannot conclude that they originate from the Sun, since magnetic clouds have clear solar eruption correspondences but small-scale flux ropes do not. There may be other plasma dynamic processes far away from the Sun that could create the small-scale flux ropes and are also modulated by the solar activity cycle.

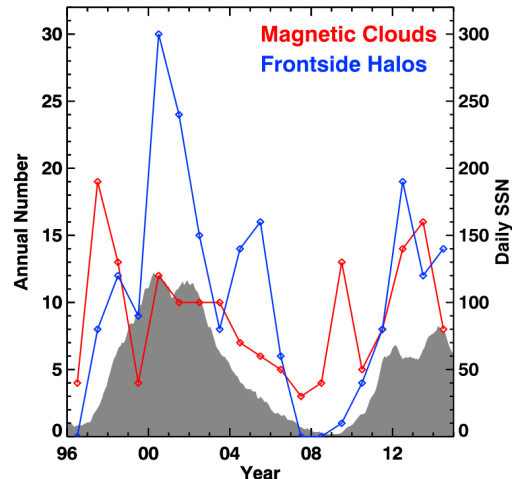


**Figure 4.3:** Occurrence counts of magnetic clouds, frontside halo CMEs and the sunspot number from 1996 to 2014 (Credit: Gopalswamy et al. [131]).

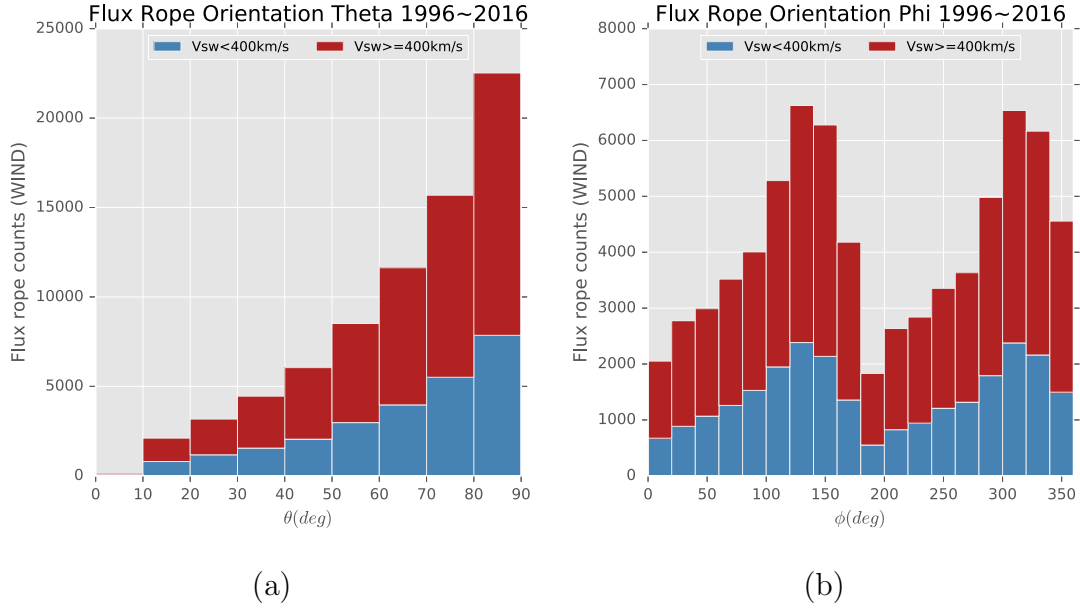
The solar cycle dependency of the small-scale flux rope occurrence rate provides weak support for the hypothesis that both small-scale flux ropes and magnetic clouds are created by solar eruptions. In the following analyses, we are going to do a more comprehensive investigation of the statistical characteristics of small-scale

flux ropes using our database, and seek for more clues on their origin and formation mechanism.

We would like to stress that what distinguishes our analysis from all previous studies is that we have far more number of events, about hundreds per month as opposed to about 1 per month, on average. Therefore, our analysis results will be based on much better statistics.

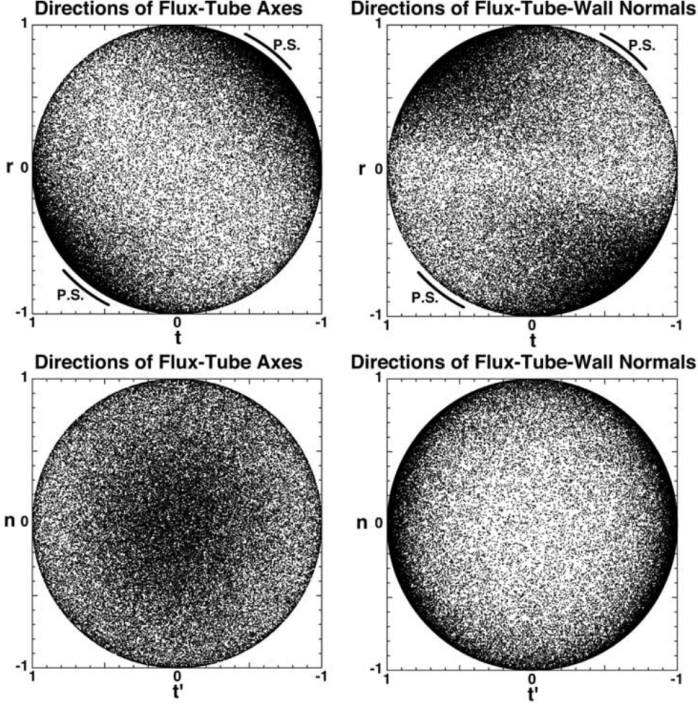
## 4.2 Axial Orientations of Small-scale Magnetic Flux Ropes

Figure 4.4 (a) and (b) show the small-scale flux rope axial orientations in the GSE spherical coordinates. Figure 4.4 (a) is the polar angle histogram which is binned by  $10^\circ$ , and Figure 4.4 (b) is the azimuthal angle histogram which is binned by  $20^\circ$ . These two plots indicate that the small-scale flux ropes have preferential axial orientations. From Figure 4.4 (a), one can see that most small-scale flux ropes have large polar angles, i.e., most of them tend to lie on the ecliptic plane. Figure 4.4 (b) shows two peaks located at bin  $120^\circ \sim 140^\circ$  and bin  $300^\circ \sim 320^\circ$ . In fact, these two bins represent two parallel but opposite directions in the GSE  $x$ - $y$  plane, so they differ by about  $180^\circ$ . Either one of these directions happens to be the tangential direction of the Parker spiral at 1 AU (corresponding to  $\phi \approx 135^\circ$  or  $315^\circ$ ). This indicates that the projection of the flux rope axis tends to align with the Parker spiral on the ecliptic plane. The red and blue bars represent the events occurring under different solar wind speed conditions (blue:  $\bar{V}_{sw} < 400$  km/s; red:  $\bar{V}_{sw} \geq 400$  km/s). Figure 4.4 (a) and (b) indicate that the small-scale flux ropes have similar axial orientation preferences in both fast and slow solar wind.



**Figure 4.4:** (a) Flux rope axial orientation: polar angle  $\theta$  histogram. The actual polar angle range is from  $0^\circ$  to  $180^\circ$ . To cut down the time consumption in flux rope detecting process, we restrict the end points of the direction vectors to be in the upper hemisphere, and do not distinguish the vectors with opposite directions from each other. (b) Flux rope axial orientation: azimuthal angle  $\phi$  histogram. This angle is measured from the positive GSE  $X$ -axis toward the projection of the flux rope axis onto the ecliptic plane.

Borovsky et al. [104] analyzed the orientations of 65,860 flux tubes from 1998 to 2004 observed by the ACE spacecraft. The wall-to-wall distances of their flux tubes were ranging from about  $10^5$  km to about  $10^7$  km, which is similar to the scale size range of the small-scale flux ropes in our database. They found that most flux tubes tend to align their axial directions with the Parker spiral. From the top left panel in Figure 4.5 [104], one can see that the tip ends of unit directional vectors of flux tube axes are accumulated near the two poles labeled by ‘‘P.S.’’, denoting the nominal Parker spiral direction. While the directions of flux-tube axes tend to align with the nominal Parker spiral direction, the flux-tube wall normals are



**Figure 4.5:** The scatter plots of three-dimensional unit vector tips of 65,860 flux tube axes observed by the ACE spacecraft in the solar wind by Borovsky et al. [104]. The time range is from the year 1998 to 2004. The three-dimensional vector tips plotted in top panels are in  $r$  versus  $-t$  coordinates, and the three-dimensional vector tips plotted in bottom panels are in a coordinate system  $(r', t', n)$  with  $r'$  along the nominal Parker spiral direction. The 2nd to 98th percentiles range of values of the expected Parker spiral directions are indicated as the short curves labeled “P.S.” (Credit: Borovsky et al. [104]).

generally perpendicular to the axial directions. Comparing Figure 4.4 (a) and (b) with Figure 4.5, we find that the orientations of both small-scale flux ropes in our database and the flux tubes examined by Borovsky [104] are consistent. This indicates that, in general, the small-scale flux ropes in our database may be considered equivalent to or to constitute a subset of the flux tubes identified by other means.

Based on the statistical results of flux tubes, Borovsky et al. [132] proposed a simple model of flux tube structure of the solar wind. In Figure 4.6, one can see the

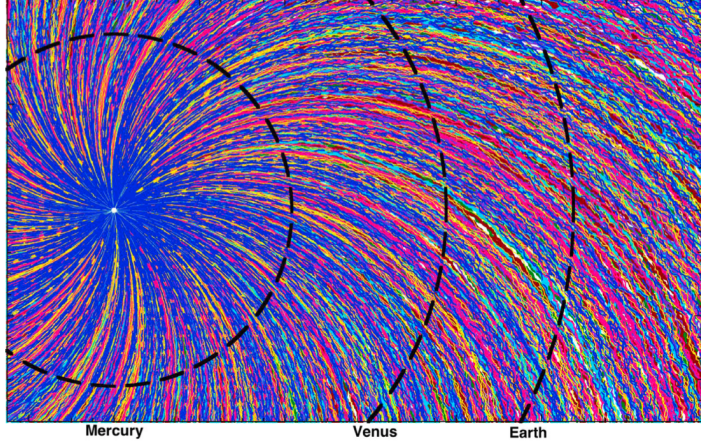
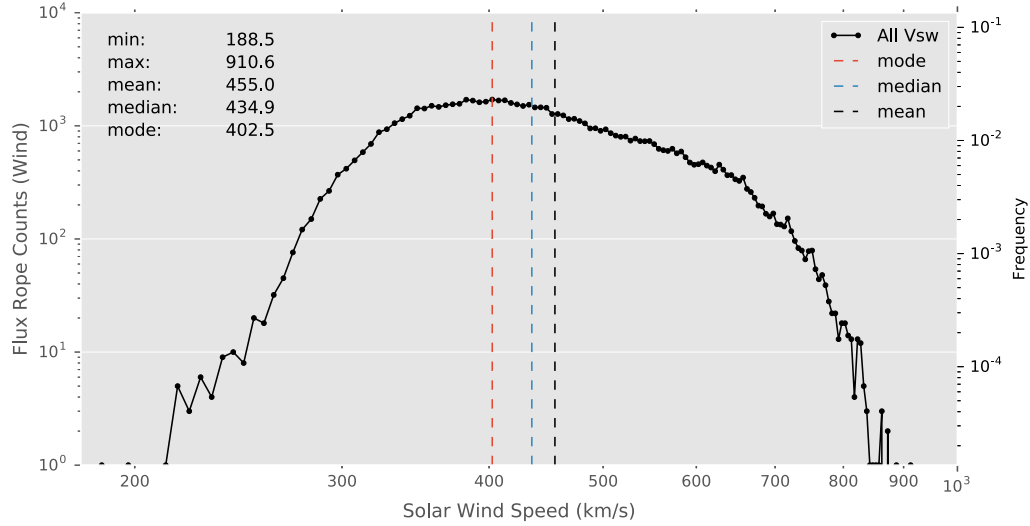


**Figure 4.6:** A depiction of the flux tube structure of the solar wind proposed by Borovsky et al. [132] (Credit: Borovsky et al. [132]).

“sea of flux tubes”. It is believed that the different bulks of plasma with different properties do not mix with each other. As a result, Borovsky argued that the plasma does not mix from one tube to the other [104, 132]. In Figure 4.6, the various colors represent the individual flux tubes in which the plasma properties are held. If such a “sea of flux tubes” exists, we can expect that a similar “sea of flux ropes” exists. The flux tubes in Figure 4.6 are occupying the whole space. However, later we will show that the statistical analyses based on our small-scale flux rope database indicate that most small-scale flux ropes are clustered and have a tendency to locate near the heliospheric current sheet. In the next section, we will discuss in detail the statistical properties of small-scale flux ropes derived from our database.

### 4.3 Statistical Properties of Small-scale Magnetic Flux Ropes

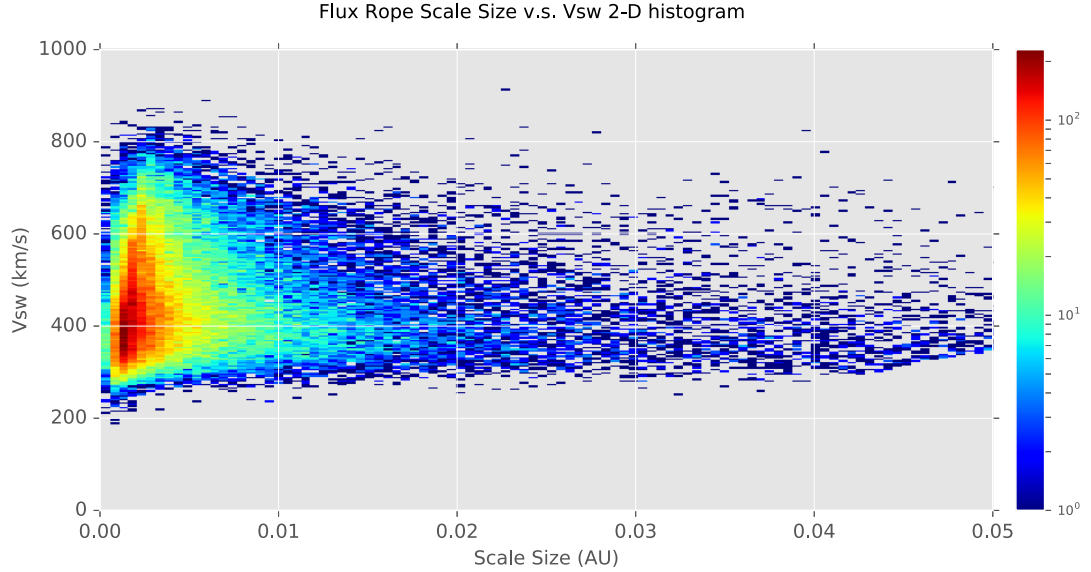
In this section, we present some statistical properties of the flux ropes in our database. First of all, we analyze the solar wind speed distribution within the flux rope intervals. Figure 4.7 shows the histogram of average solar wind speed  $\bar{V}_{sw}$  within each flux rope interval. One can see a peak near  $\bar{V}_{sw} = 400$  km/s (the mode of the distribution is 402 km/s) and three approximately linear sections on the curve with different slopes in this log-log plot. The first section of the curve is from  $\bar{V}_{sw} = 200$  km/s to  $\bar{V}_{sw} = 400$  km/s. The slope of the first section is positive. The second section of the curve is from  $\bar{V}_{sw} = 400$  km/s to  $\bar{V}_{sw} = 650$  km/s, with negative slope. The third section of the curve is from  $\bar{V}_{sw} = 650$  km/s to  $\bar{V}_{sw} = 900$  km/s, with steep negative slope. Three distinct slopes in the log-log plot indicate three distinct power law distributions with different power indices. Since the solar wind speed is a key factor in space plasma dynamic processes, different power law distributions may imply different flux rope generation mechanisms for different plasma flow streams. Therefore, in the following analyses, we split the entire database into two subsets according to the corresponding average solar wind speed either greater or less than 400 km/s. Note that this value is also close to the mode of the distribution, 402 km/s, corresponding to the peak in the histogram of average solar wind speed (Figure 4.7). The median of this distribution is 435 km/s, indicating that a division at 400 km/s approximately separates the database into two subsets of about half the total number of events.



**Figure 4.7:** The histogram of average solar wind speed within small-scale flux ropes.

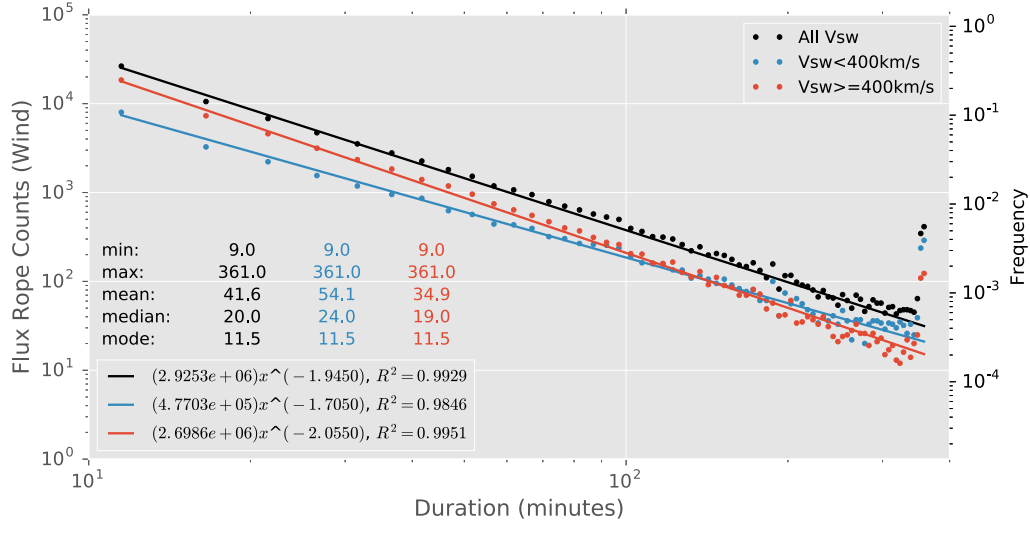
Figure 4.8 is the 2-D histogram of flux rope  $\bar{V}_{sw}$  *versus* scale size. It shows that the flux ropes with larger scale sizes tend to occur in slow solar wind ( $\bar{V}_{sw} \approx 400$  km/s). For the shorter scale size flux ropes, the associated solar wind speed spreads widely (from about 200 km/s to about 800 km/s). The line of  $\bar{V}_{sw} = 400$  km/s divides the plotted shape into two triangles. Above the line of  $\bar{V}_{sw} = 400$  km/s, the solar wind speed goes down as the scale size increases, while below the line of  $\bar{V}_{sw} = 400$  km/s, the solar wind speed goes up as the scale size increases. This plot is another basis based on which we split the entire dataset at  $\bar{V}_{sw} = 400$  km/s.

Figure 4.9 (a) and (b) show the durations and scale size distributions of small-scale flux ropes in our database. The data points in black in each plot represent the histogram of the entire event set, and the points in blue and red represent the histograms of the subsets for slow ( $\bar{V}_{sw} < 400$  km/s) and fast ( $\bar{V}_{sw} \geq 400$  km/s) solar wind speed, respectively. In Figure 4.9 (a), the shapes of these three curves are

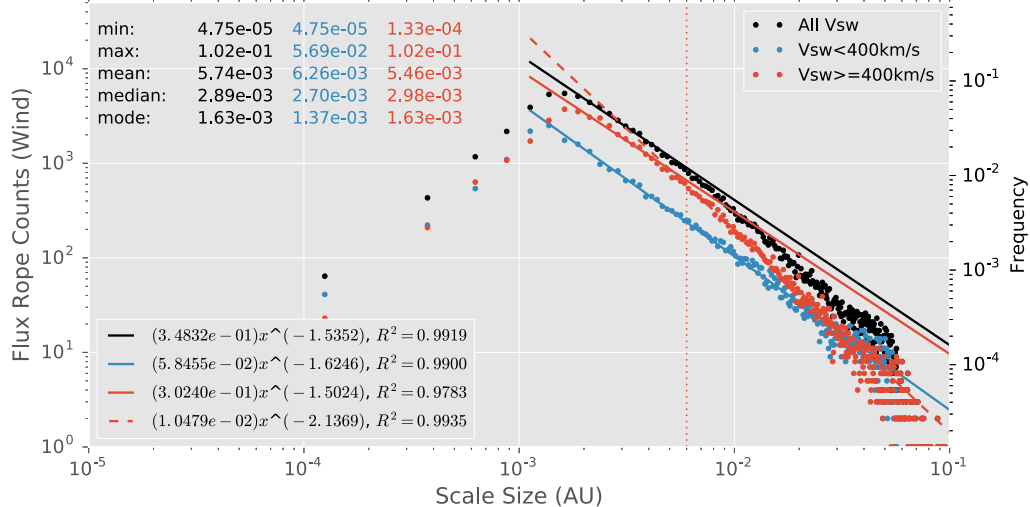


**Figure 4.8:** The 2-D histogram of flux rope average solar wind speed ( $\bar{V}_{sw}$ ) *versus* scale size.

close to straight lines on the log-log scale except for the high tails to the right. After examining the generation process of our flux rope database, we find that the high tail is due to cutoff effect of a finite range of sliding window widths. As described in Chapter 3, the last step of the flux rope detecting process is to combine all flux rope candidate lists with different duration ranges. In this process, some shorter duration flux ropes will be absorbed into the longer duration flux ropes which enclose the former. In the present database, the longest duration range is 354~361 minutes, which means that the flux ropes within this duration range will not be merged into longer flux ropes, because there are no longer durations allowed beyond this range, thus the cutoff. Actually, the flux ropes in duration ranges shorter than 354~361 minutes may also be enclosed by longer flux ropes with durations beyond 354~361 minutes. This cutoff leads to the enhanced fluctuation and a high tail near the end



(a)



(b)

**Figure 4.9:** (a) The histogram of small-scale flux rope duration plotted in logarithmic scales. The time range is from 9 minutes to 361 minutes, with 5 minutes bin size. Note that the high tails to the right ends of the curves are due to duration boundary cutoff effect (see explanations in text). (b) The histogram of small-scale flux rope cross section scale sizes plotted in logarithmic scales, with 0.00025 AU bin size. The flux rope scale size is calculated from the flux rope duration taking into account the axial orientation. Again, the low points to the left and right ends of the curves are due to boundary cutoff effect. For both (a) and (b), the basic statistical properties and linear regression parameters for each curve are listed, respectively.

to the right. To support this explanation, we manually shifted the cutoff boundary to shorter durations, and the high tail also shifted accordingly. In Figure 4.9 (b), there are low tails at both ends in each curve, which are also caused by the same cutoff effect of finite duration ranges. Due to the boundary cutoff in duration ranges, when converting the duration to scale size, there is a lack of events near the lower and upper scale size boundaries. We exclude these abnormal sections of the data points in the subsequent analyses.

Except for the high tails due to the cutoff effect, Figure 4.9 (a) shows a linear relation between the flux rope occurrence counts and the duration under logarithmic scales, which indicates a power law distribution of flux rope duration. The color coded straight lines are the corresponding fitted power law functions as denoted. The flux ropes under the slow solar wind condition obey the power law with a power index  $\sim -1.71$ , while the ones in fast solar wind obey the power law with a power index  $\sim -2.06$ . One can see that the red curve ( $\bar{V}_{sw} \geq 400$  km/s) has larger absolute slope value than the blue curve ( $\bar{V}_{sw} < 400$  km/s). The intersection of the blue and red curves is located at about 120 minutes. To the left side of the intersection point, there are more flux rope events with fast solar wind speed, while to the right, there are more flux rope events with low solar wind speed. This indicates that the longer duration flux ropes (duration  $> 100$  minutes) tend to occur under the slow solar wind speed condition.

Figure 4.9 (b) also exhibits approximately linear relations (in logarithmic scales) between flux rope scale size and occurrence counts, excluding the low ends due to the cutoff effect. This indicates a power law distribution of flux rope scale

sizes, properly calculated by taking into account the axial orientations. At a glance, the absolute slope of the red curve ( $\bar{V}_{sw} >= 400$  km/s) is greater than that of the blue curve ( $\bar{V}_{sw} < 400$  km/s), which is consistent with Figure 4.9 (a). In other words, the power law slope of the red curve is softer than the blue curve. Comparing with Figure 4.9 (a), one can see that the flux ropes ranging from 9~361 minutes have the approximately corresponding scale-size range of 0.002~0.05 AU (excluding the lower end). When we use power law functions to fit the data, we find that the data points in blue color are fitted very well by a single power law function with a power index  $\sim -1.62$ , but for the red and black data points, the tails show noticeable deviations from a single fitted line. Apparently, the deviations in the black data points are due to the deviations in the red ones. We use two power law functions with different power indices to fit the red data points, and find that in the scale size range  $0.001 \sim 0.01$  AU, the red data points are well fitted by a power law function with a power index  $\sim -1.50$ , while in the range  $0.01 \sim 0.05$  AU, the red data points are well fitted by a power law function with a power index  $\sim -2.14$ . The breakpoint of the two power laws is at  $\sim 0.006$  AU.

It is interesting to note that both Figure 4.9 (a) and (b) obey the power law distribution. Because the flux ropes can take any axial orientations, it is not guaranteed that a longer duration corresponds to a larger scale size. However, in Figure 4.9 (a) and (b), since both of these two quantities obey the power law, they may have a simple linear relationship. To verify this relationship, we plot the 2-D histogram for flux rope duration and scale size in Figure 4.10. Figure 4.10 (f) shows that there do exist cases in which the shorter duration flux ropes have larger scale

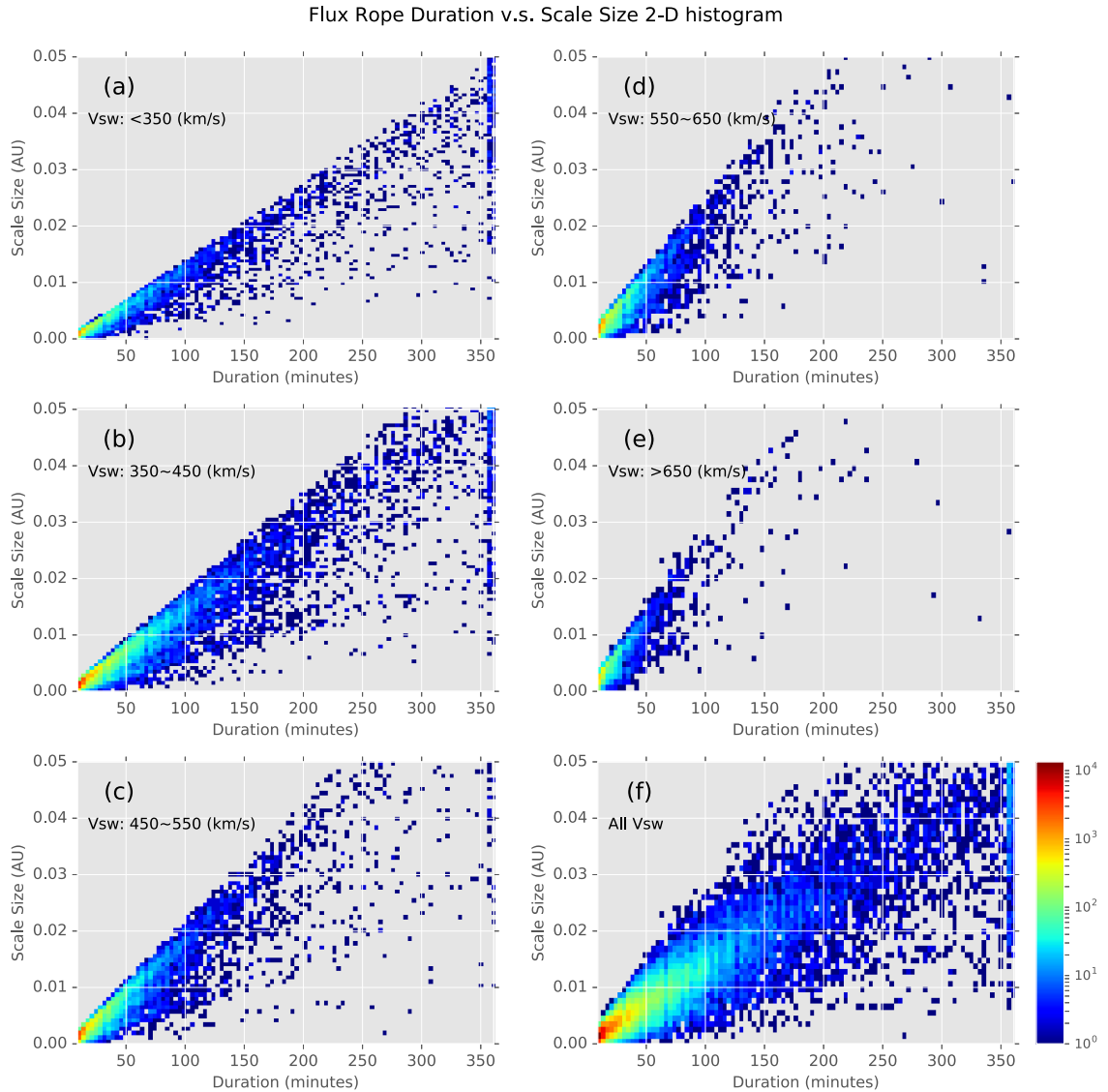


**Figure 4.10:** The 2-D histogram of flux rope scale size *versus* duration. The bin grids are  $100 \times 100$ . Subplots (a) to (e) are histograms under different solar wind speeds, and subplot (f) is the histogram for the entire dataset. The color bar represents the corresponding small-scale flux rope counts.

sizes, or vice versa, but the overall trend is that the flux rope scale size is roughly proportional to the flux rope duration, although not exactly linear. Apparently, the progression of the lift of the upper bound in scale sizes from panels (a) to (e) in Figure 4.10 is due to the increasing solar wind speed. The power law distributions are fairly common in nature. These analysis results are relatively new, concerning small-scale flux ropes. We will explain these new results in the following paragraphs from the perspective of self-organized criticality theory.

The self-organized criticality (SOC) theory was first proposed by Bak et al. [133], and then applied by Lu et al. [134, 135] to solar physics to explain the power law distributions of flare occurrence rate over flare energy, peak flux, and duration. This model is usually referred to as the avalanche model and has been widely used to explain the statistical characteristics of hard x-ray (HXR) flares [135–138]. The avalanche model predicts a power law distribution for the total energy, the peak luminosity, and the duration of individual events. Li et al. [139] studied the solar flares and CMEs during the solar cycle 23. They found that the solar flare duration distribution obeys a power law with a power index  $\sim -2.55$ . In Figure 4.9 (a), we also produce a power law, implying that the occurrence of small-scale flux ropes may be explained by the SOC theory. Note that the absolute values of the power indices from our fitted functions are generally smaller than those in Li et al.'s [139] result, since solar flares or CMEs and small-scale flux ropes probably belong to two different kinds of processes. Although they share similar statistical characteristics in terms of the power law distributions in certain quantities, complying with the SOC theory, the

underlying physical mechanism responsible for generating such behavior still cannot be revealed.

The flux rope size computed from flux rope duration and its axial orientation may have better correspondence to flare duration. Here we apply a tentative assumption that a portion of small-scale flux ropes comes from the Sun and has some direct relation to solar eruptions (i.e., flares and CMEs). If this is true, their distribution functions should have some similarity. We also assume that the duration of flares corresponds to the scale size of small-scale flux ropes. Based on this idea, let us look back to the fitted distribution functions in Figure 4.9 (b). The blue data points and the fitted line show that all the flux ropes in slow solar wind obey the power law with a power index  $\sim -1.62$ , whereas there is a break point in the power law fitting to the red data points at  $\sim 0.01$  AU. The power index in the larger scale size range  $0.01 \sim 0.05$  AU is  $\sim -2.14$ , which is closer to the power index for the flare duration distribution in Li et al. [139] ( $\sim -2.55$ ), and that for the flare peak flux ( $\sim -2.13$ ). We speculate that the larger scale size flux ropes ( $0.01 \sim 0.05$  AU) in our database under the condition of relatively high speed solar wind ( $\bar{V}_{sw} \geq 400$  km/s) may have closer relation to solar source than the small-scale flux ropes under all other conditions.

Figure 4.11 (a) is the histogram of average proton temperature within flux ropes plotted in logarithmic scales. We can see that the peaks of blue and red curves are separated, corresponding to different modes. The peak of the red curve ( $\bar{V}_{sw} \geq 400$  km/s) is near  $\bar{T}_p \approx 0.1 \times 10^6$  K, while the peak of the blue curve ( $\bar{V}_{sw} < 400$  km/s) is near  $\bar{T}_p \approx 0.03 \times 10^6$  K. Therefore, the small-scale flux ropes

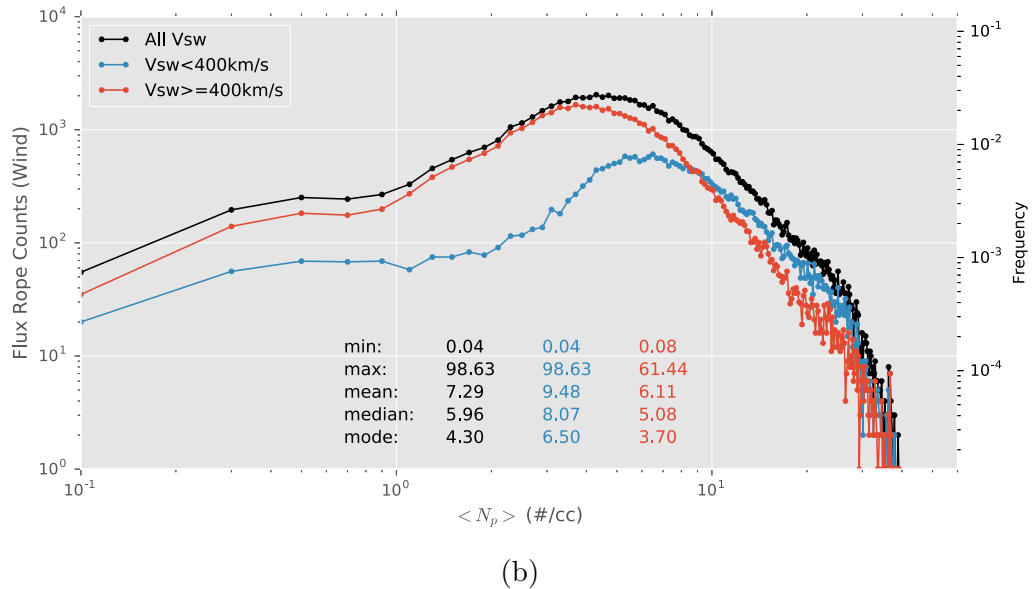
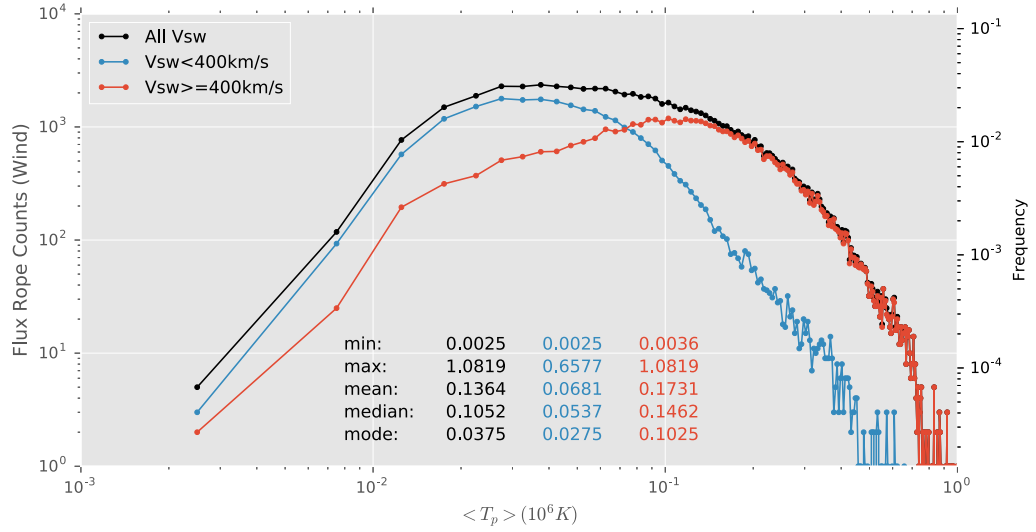
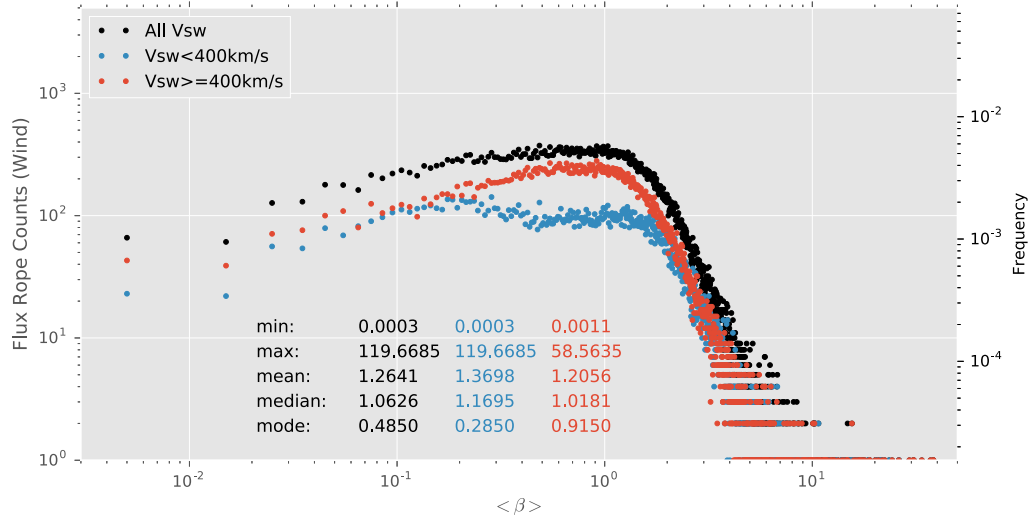


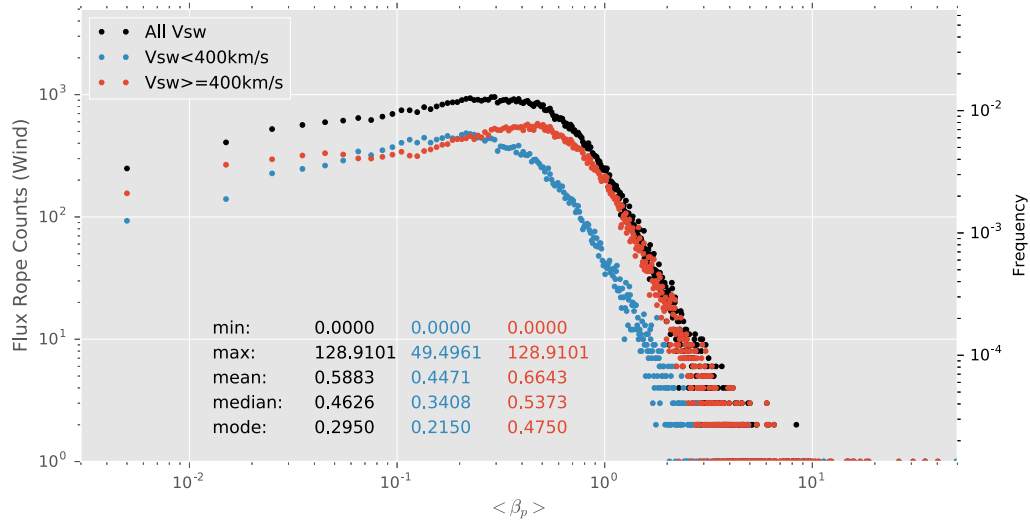
**Figure 4.11:** (a) The histogram of average proton temperature within flux ropes in logarithmic scales, with  $0.005 \times 10^6$  K bin size. (b) The histogram of average proton number density within flux ropes in logarithmic scales, with  $0.2 \#/\text{cc}$  bin size. For both (a) and (b), the blue curve represents the flux rope events under solar wind speed  $\bar{V}_{sw} < 400$  km/s, and the red curve with solar wind speed  $\bar{V}_{sw} \geq 400$  km/s. The black curve represents the entire event set.

under low speed solar wind ( $\bar{V}_{sw} < 400$  km/s) tend to have low proton temperature, while the ones under medium and high speed solar wind ( $\bar{V}_{sw} \geq 400$  km/s) tend to have high proton temperature. Note that the black curve and the red curve are overlapping beyond  $\bar{T}_p = 0.2 \times 10^6$  K, which means that the small-scale flux ropes with proton temperature greater than  $0.2 \times 10^6$  K occur predominantly under medium and high speed solar wind conditions. Figure 4.11 (b) is the histogram of average proton number density within flux ropes plotted in logarithmic scales. Note that the appearance in Figure 4.11 (b) is opposite to that in Figure 4.11 (a). In Figure 4.11 (b), the flux ropes under medium and high solar wind speed tend to have lower proton number density, while the flux ropes in slow solar wind tend to have higher density. To summarize Figure 4.11 (a) and (b), the flux ropes in slow speed solar wind tend to have low proton temperature and high proton number density, while the flux ropes in medium and high speed solar wind tend to have high proton temperature and low proton number density.

Figure 4.12 (a) is the histogram of average plasma  $\beta$  (electron temperature  $T_e$  included) within flux ropes plotted in log-log scales. The black curve shows that the occurrence counts of all small-scale flux ropes are significant at  $\bar{\beta} = 1$ . The red curve has the same trend as the black curve, while the blue curve has a flat top. From the shapes of these curves, we find that the numbers of small-scale flux rope with  $\bar{\beta} < 1$  and the ones with  $\bar{\beta} > 1$  are about the same (medians  $\sim 1$ ). However, in magnetic clouds, the magnetic pressure always dominates over thermal pressure, which causes ultra low plasma  $\beta$  (or  $\beta_p$  below). Figure 4.12 (b) is the histogram of average proton plasma  $\beta_p$  (excluding  $T_e$ ) within flux ropes plotted in log-log scales.



(a)



(b)

**Figure 4.12:** (a) The histogram of average plasma  $\beta$  within flux ropes, with bin width 0.01. (b) The histogram of average proton plasma  $\beta_p$  within flux ropes, with bin width 0.01. For both (a) and (b), the blue curve represents the flux rope events with solar wind speed  $\bar{V}_{sw} < 400$  km/s, and the red curve with solar wind speed  $\bar{V}_{sw} \geq 400$  km/s. The black curve represents the entire event set.

Because the electron temperature data quality is generally poor. They are not always available. To overcome the large data gaps in  $T_e$ , we also plot the histogram of the average proton plasma  $\beta_p$ , in which only the contribution of proton temperature  $T_p$  is included when calculating the thermal pressure (see Equation (2.28)). The distributions in Figure 4.12 (b) are similar to those in Figure 4.12 (a). All curves in Figure 4.12 (b) are shifted to the left compared with Figure 4.12 (a), indicating that the plasma  $\beta$  is significantly enhanced by the electron temperature contribution, as also indicated by the various statistical quantities denoted on each plot.

The low proton temperature ( $T_p$ ) is a key characteristic of magnetic clouds. However, for small-scale magnetic flux ropes, the  $T_p$  varies case by case. Figure 4.13 is the 2-D histogram of flux rope temperature  $T_p$  *versus* scale size. The triangle shape distribution stretching down to the right in Figure 4.13 (f) indicates that the flux ropes with larger scale size ( $\geq 0.02$  AU) usually have lower  $T_p$  ( $\leq 0.1 \times 10^6$  K). Given that the large-scale magnetic flux ropes (MCs) have low  $T_p$ , this seems to be a smooth transition from the small-scale magnetic flux ropes to their larger counterparts. For the smaller size small-scale flux ropes, the range of  $T_p$  spreads widely. Figure 4.13 (f) shows that the range of  $T_p$  of the flux ropes with scale size less than 0.05 AU spreads from near 0 to  $0.8 \times 10^6$  K. When looking into the distribution under different solar wind speed conditions, we find that most of the relatively larger size small-scale flux ropes ( $\geq 0.02$  AU) appear in the slow solar wind with low  $T_p$  (see Figure 4.13 (a), (b), and (c)). As for the relatively smaller size small-scale flux ropes ( $\leq 0.01$  AU), they appear in both fast and slow solar wind. The different locations of the high frequency regions (in red and yellow colors) in each subplot show that the flux ropes

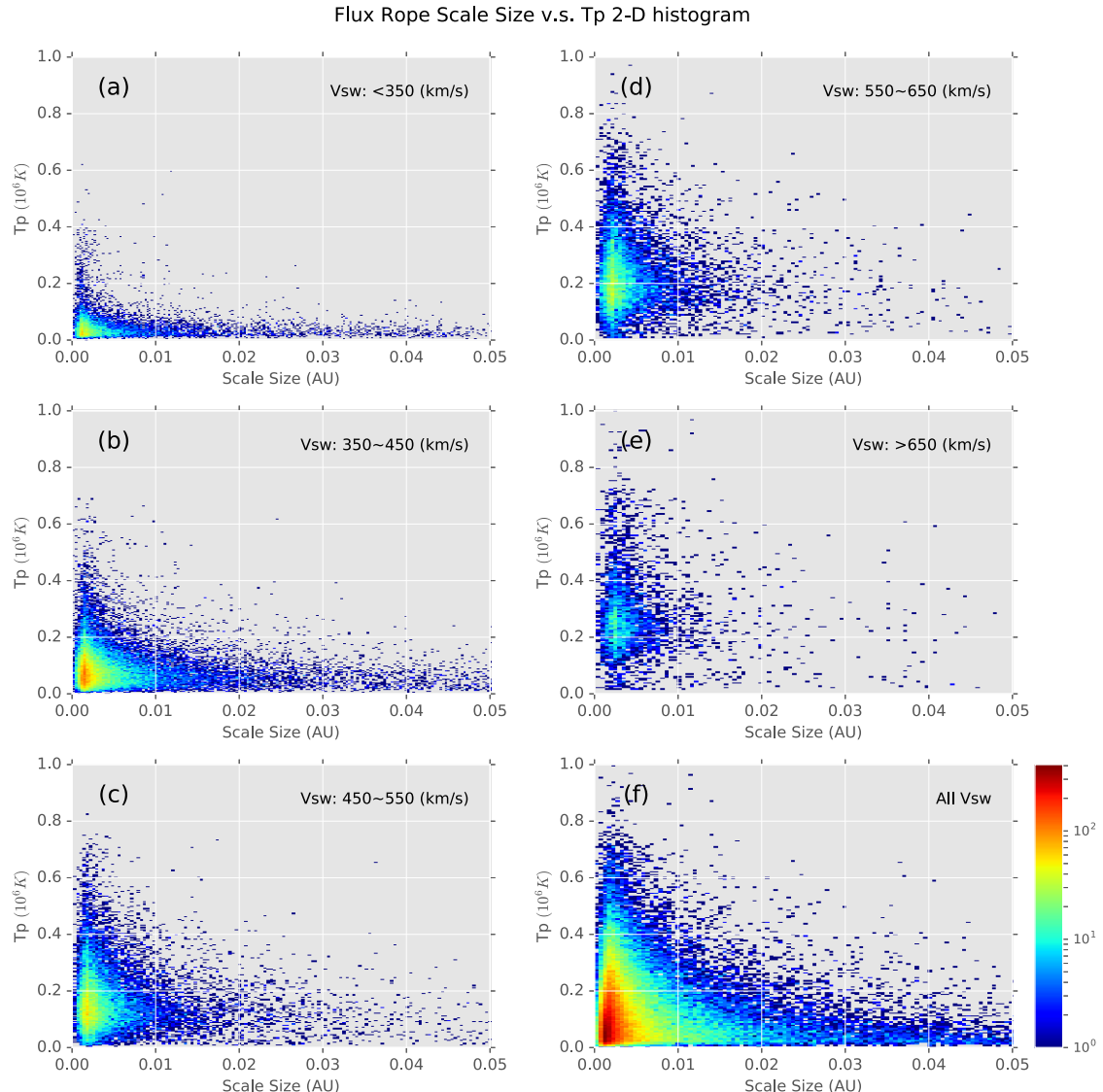


**Figure 4.13:** The 2-D histogram of flux rope proton temperature *versus* scale size. The bin grids are  $200 \times 200$ . Subplots (a) to (e) are histograms under different solar wind speeds, and subplot (f) is the histogram for the entire dataset. The color bar represents the small-scale flux rope counts.

in high (low) speed solar wind tend to have higher (lower) proton temperature, which is consistent with the result shown in Figure 4.11 (a).

#### 4.4 Waiting Time Distribution Analysis on Small-scale Magnetic Flux Ropes

The waiting time distribution (WTD) is defined by the distribution of time intervals or separations between discrete events. The WTD of the successive discrete events reveals whether they occur independently. Many models on solar eruptive processes predict definitive WTDs, so the WTD analysis based on observational data is a powerful tool to validate these models. The WTD analysis is widely used in statistical analyses of space plasma processes such as CMEs [139], solar flares [139, 140], current sheets [141], gamma ray burst [142], solar energetic particles [143], and also in other discrete time random processes such as earthquakes [144]. In this section, we apply the WTD analysis to small-scale magnetic flux ropes, in order to investigate the underlying mechanism governing the flux rope origination process. We discuss the possible implications on the flux rope origination by comparing the WTDs of flux ropes with the WTDs of some relevant processes, especially those from the analysis of current sheets [97, 106, 141, 145].

As predicted by the avalanche model [133–135], the occurrence of solar flares is a Poisson process, i.e., the flare WTD is a single exponential function in waiting time,  $\Delta t$ . In fact, the occurrence rate of many processes is non-constant, and as an observational result, the flare WTD sometimes shows time-dependent Poisson distributions [139, 146–149]. However, some observational results showed deviations

of the flare WTD from a pure Poisson process. Pearce et al. [150] studied 8319 HXR solar flares during solar minimum (1980  $\sim$  1985), and pointed out that the WTD ( $\Delta t$  ranging from 0 to 60 minutes) of flares has large deviation from a stationary Poisson process, but is well fitted by a power law function with a power index -0.75 (See Figure 4 in Pearce et al.’s paper [150]), indicating the flares did not occur purely randomly. Li et al. [139] investigated the statistical properties of CMEs and solar flares during solar cycle 23. They adopted the non-stationary Poisson distribution functions from Li et al. [143] and Guidorzi et al. [149] to fit the WTDs of solar flares and CMEs, and obtained good fitting results. In Li et al.’s [143] and Guidorzi et al.’s [149] non-stationary Poisson distribution functions, the asymptotic behavior of the longer waiting time in the tail leads to power law functions for long waiting time.

In this section, we try various fitting functions mentioned above to fit the flux ropes WTDs. Primarily we use exponential and/or power law function fittings to yield the optimal result as we present below. The functions used by Li et al. [143] and Guidorzi et al. [149] based on non-stationary Poisson distribution do not work, partially due to the limited range of waiting times,  $\Delta t$ , in our analysis. Here we use two different kinds of definition for waiting time [151]. The first kind of waiting time is defined by the time from the end of one flux rope interval to the start of the next one, i.e., the time interval between adjacent flux ropes. And the second kind of waiting time is defined by the time from the starting time of one flux rope to the starting time of the next, i.e., the time interval between the starting times of two successive flux ropes.

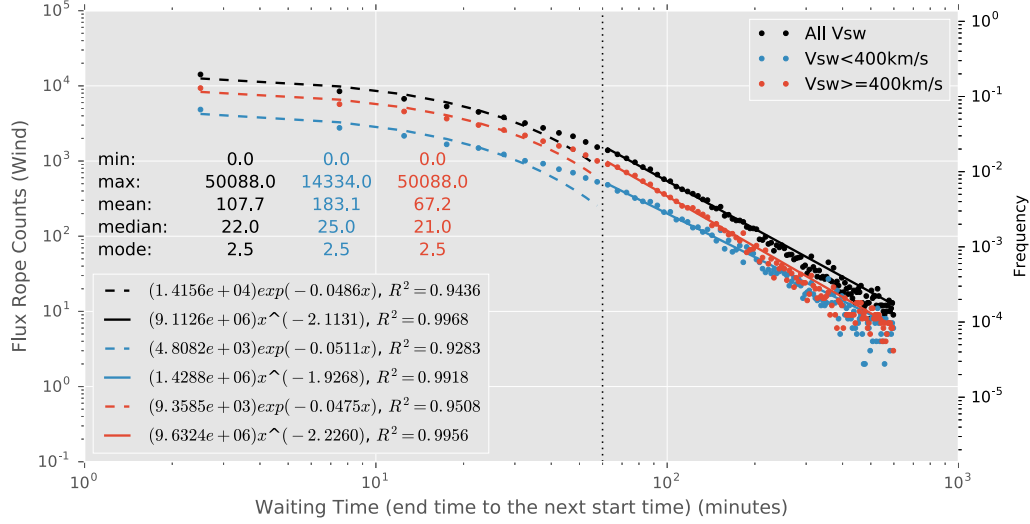


**Figure 4.14:** The waiting time distribution (1st kind) of small-scale magnetic flux ropes. In this plot, the waiting time is defined by the interval between the end time of one flux rope to the start time of the next one. The dots in black represent the entire data set, and the dots in blue and red represent the subsets under low solar wind speed ( $\bar{V}_{sw} < 400$  km/s) and medium as well as high solar wind speed ( $\bar{V}_{sw} \geq 400$  km/s), respectively. The bin size is 5 minutes, and the data point for each bin is located in the bin center. The dashed lines are fitted curves by exponential functions, and the solid lines are fitted curves by power law functions. The dotted vertical line denotes the break point, which is located at 60 minutes. The basic statistics and fitting parameters are denoted, where the function forms and the fitting quality metric  $R^2$  are listed.

Figure 4.14 is the flux rope WTD of the first kind. For each color-coded data set, we use an exponential function to fit the data points with waiting time less than 60 minutes. The exponential function fits the data well where waiting time is less than 40 minutes. Then the deviation grows as the waiting time becomes larger. The section beyond 60 minutes is fitted by a power law function. The power law function fits the tail very well, with  $R^2 > 0.99$  for each data set. An exponential WTD indicates a random Poisson process of the event occurrence, while a power law WTD suggests the clustering behavior of the events. The fitting results show that

the overall WTD shown in Figure 4.14 is neither a single Poisson distribution nor a power law distribution.

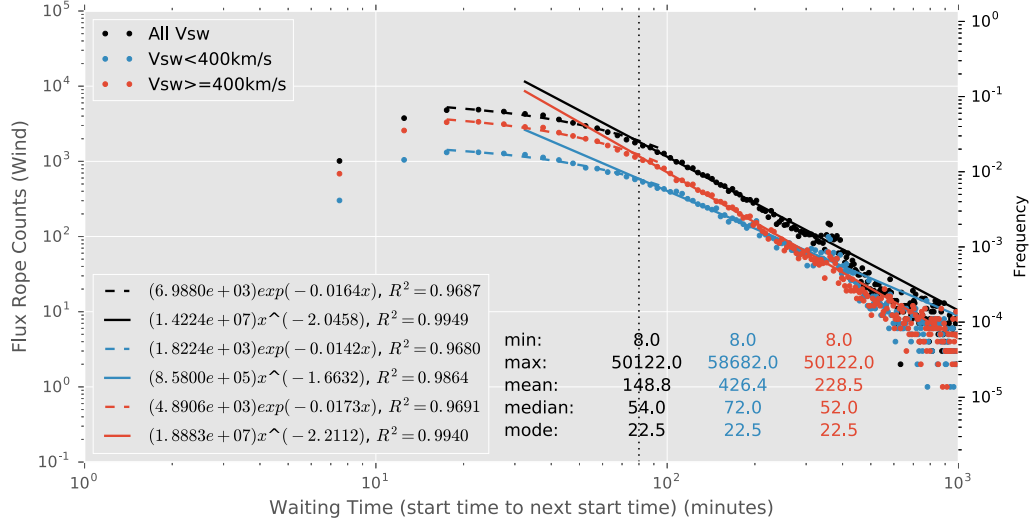


**Figure 4.15:** The waiting time distribution (2nd kind) of small-scale magnetic flux ropes. In this plot, the waiting time is defined by the interval between the start time of one flux rope to the start time of the next one. The format is the same as in Figure 4.14. The vertical dotted line is at 80 minutes.

Considering that the starting time of one flux rope may correspond to the onset of solar eruptive process back on the Sun, according to the definition by Wheatland et al. [147], we perform the WTD analysis based on an alternative definition of waiting time. In this definition, the interval between two consecutive starting times is considered as the waiting time. As mentioned previously, we call the WTD under this definition the WTD of the second kind. Figure 4.15 shows the flux rope WTD of the second kind. One can notice the outliers near the two ends. The outliers on the tail are located between 300 minutes to 400 minutes, which is the same location as the outliers appearing in Figure 4.9 (a) and (b). Apparently, these outliers are due

to boundary cutoff effect. As for the outliers with the shortest waiting time, we also attribute them to boundary cutoff effect. Because in our database, the minimum flux rope duration is set at  $\sim 9$  minutes, there are no flux rope events with durations less than 9 minutes. However, the separation between two flux ropes can be of any time duration. When we use the definition of the first kind, the shortest waiting time can be zero, but for the definition of the second kind, the shortest waiting time has to be  $\sim 9$  minutes. As a result, there is a lack of events with short waiting time in the WTD of the second kind. Excluding these bias, we apply the same fitting procedures as in Figure 4.14. In Figure 4.15, for each curve, we can see that the section less than 80 minutes is well fitted by an exponential function, and the section greater than 80 minutes is well fitted by a power law function. The exponential fittings in Figure 4.15 are better than those in Figure 4.14, indicating that the events associated with short waiting time ( $< 80$  minutes) are subject to the simple Poisson process, while the ones associated with longer waiting time ( $> 80$  minutes) seem to have clustering behavior. The combination of an exponential and a power law distribution implies that there may be two distinct mechanisms underlying the event occurrence.

It is worth noting that the fitting result given in Figure 4.15 is similar to the result on current sheets WTD obtained by Bruno et al. [106] and Miao et al. [141]. Bruno et al. [106] showed an exponential fitting to the waiting time of intermittent events (current sheets) identified from the Helios 2 spacecraft at 0.9 AU in a high speed solar wind stream. The exponential fit persisted for a range of waiting time between 12 minutes and  $\sim 2$  hours, compatible with the exponential-fitting range of  $\Delta t$  in Figure 4.15. Miao et al. [141] studied the statistical characteristics of current

sheets observed by the Ulysses spacecraft in 1997, 2004, and 2005 (also including a few days in 1996 and 2006). They found that the current sheets WTD can be well fitted by an exponential function and a power law function as well. However, the break point in Miao et al.'s fitting is at  $\sim e^{10}$  seconds (367 minutes) (see Figure 9 in Miao et al.'s paper [141]), and the power law index is -1.85, which is different from the power law index in our results ( $\sim -2.05$  for all events and  $\sim -2.21$  for high speed solar wind in Figure 4.15). A word of caution is that Miao et al.'s [141] results were obtained from Ulysses observations near the ecliptic plane, but at radial distances  $\sim 4\text{-}5$  AU from the Sun. Therefore significant evolution, at least passively, may have contributed to the difference between the two sets of results obtained at different heliocentric distances. Although not totally comparable, the similar piecewise behaviors of the flux rope WTD and the current sheet WTD imply that they may share similar generation mechanisms or have some kind of association.

Boffetta et al. [152] investigated the HXR flares between 1976 and 1996. They found that the WTD of these flares showed consistency to a power law distribution with a power index  $\sim -2.4$  (the waiting time ranges from 6 hours to 67 hours). Lepreti et al. [153] re-analyzed 25-year worth GOES flare list (1975  $\sim$  1999), and obtained good fitting by the Lévy function, in which the WTD obeys a power law at large values of waiting time, in the range  $3 \sim 11$  hours with a power index  $\sim -2.4$ . As pointed out by Lepreti et al. [153], the asymptotic power law with a power index  $\sim -2.4$  is very robust. In our result, the power index for flux rope WTD in Figure 4.15 for the entire dataset (black curve) is  $\sim -2.05$ , somewhat similar to Boffetta et al.'s [152] and Lepreti et al.'s [153] results. Deviations may be due to the different ranges of waiting

time in different studies. Li et al. [139,143] examined WTDs for solar energetic proton events, type II radio bursts, solar flares, and CMEs, and obtained a power law index,  $\sim -2$ , for longer waiting time in each distribution.

We also tried the same method as Li et al. [139] did in fitting the WTDs of solar flares and CMEs. However, in both Figure 4.14 and Figure 4.15, the non-stationary Poisson distribution function gives poor fitting, indicating that at least for the range of waiting time considered in the present analysis, the WTDs probably are not readily explained by the non-stationary Poisson distributions advocated by Li et al. [139].

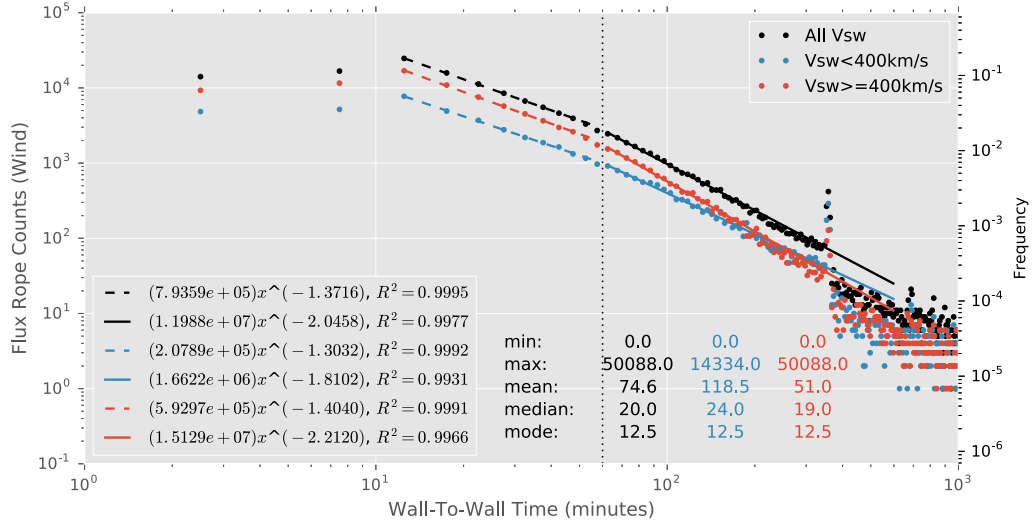


**Figure 4.16:** The wall-to-wall time distribution of small-scale magnetic flux ropes. The walls correspond to flux rope boundaries. Format is the same as Figure 4.14. The dashed lines and the solid lines are all fitted by power law functions with different power indices. The dotted vertical line denotes the break point, which is located at 60 minutes.

Greco et al. [97,151] showed the consistency between the WTDs of the solar wind discontinuities observed by the ACE spacecraft at 1 AU and the WTDs of

MHD turbulence simulations, suggesting that the solar wind magnetic structures may be created locally by MHD turbulence. Here the structures referred to by Greco et al. consist of “small random currents”, “current cores” (i.e., flux ropes), and “intermittent current sheets” [97, 145]. In their study, the WTD of MHD simulation result agrees well with the WTD of ACE observational data in the short waiting time range ( $< 50$  minutes, the correlation length scale of solar wind turbulence [97, 154]). For the departure from the power law beyond 50 minutes, they attributed that to the limited length scales of the computational domain, thus no large-scale features were included in the MHD simulations. In the general space plasma scenario, the current sheets can be considered as boundaries of flux ropes with negligible thickness. To make a direct comparison with the WTD of current sheets in Greco et al’s study [97, 151], where the current sheets were identified with zero thickness, we provide a proxy to those current sheets from our small-scale magnetic flux rope database. Considering that the flux ropes are bounded by current sheets, we can assume that there are current sheets existing at the starting time and the end time of each flux rope interval. We call these “current sheets” flux rope walls. Then the time interval between adjacent walls can be considered as a proxy to the waiting time of current sheets.

In practice, this is simply implemented by calculating the waiting time between these walls (note that for the walls of zero width, the two kinds of waiting time introduced earlier become the same). We call it the wall-to-wall time distribution, which is essentially the distribution of the duration and the waiting time of the 1st kind merged. Figure 4.16 is the wall-to-wall time distribution of small-scale flux ropes.

Similar to Figure 4.15, there are also outliers in Figure 4.16 due to boundary cutoff effect. In Figure 4.16, excluding those end points, one can see that for each set of points, the wall-to-wall time distribution is well fitted by two power law functions of different power indices, with a break point located at  $\sim 60$  minutes. The WTDs of the observed solar wind discontinuities in Greco et al.’s [97] paper showed that the WTD of discontinuities obeys the power law within the break point at 50 minutes (typical correlation length scale), which is consistent with our result. In addition, the power law index from Greco et al. [151] is  $-0.92 \pm 0.03$  from numerical simulation, and  $-1.23 \pm 0.03$  from the in-situ spacecraft observations at 1 AU. They compare well with our result,  $-1.37$  for the dashed black line in Figure 4.16. We note that for the case including additional flux rope events by relaxing the criterion on  $|\bar{B}|$  to  $|\bar{B}| > 0$ , the number of events doubles and the power law fitting to the wall-to-wall time persists. The index is  $-1.22$ , which is closer to  $-1.23 \pm 0.03$ . Note that for the sections beyond the break point, each is still well fitted by a power law function with a power index  $\sim 2$ , complying with the indices discussed previously. However whether these flux ropes are of different origin has yet to be seen. One may argue that the proxy to the current sheet is questionable. However, by checking the number of events we identify in Table 3.2, on average, we have  $\sim 3500$  flux ropes a year. Such an occurrence rate is comparable to that from direct current sheet identifications (keeping in mind that there are two walls with each flux rope), e.g.,  $\sim 10,000$  a year from Miao et al. [141], especially for events associated with smaller waiting time. In addition, in the process of determining the boundary of a flux rope, we are looking for similar type of a discontinuous behavior in both the plasma and magnetic

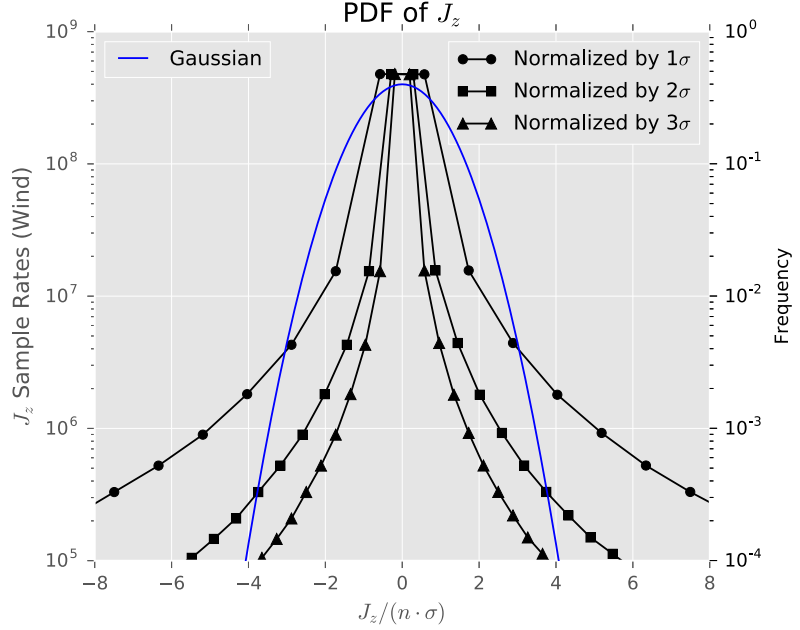


**Figure 4.17:** PDF of the axial electric current density inside the small-scale magnetic flux ropes derived from our database. The original current density values are binned by  $0.01 \times 10^{-9}$  Ampere/m<sup>2</sup>. The three black curves with different markers are normalized by different multiples of the standard deviation. The blue curve is the standard Gaussian distribution. This PDF takes into account all small-scale flux ropes, including the ones with average magnetic field magnitude less than 5 nT.

field parameters, e.g., a break or a mismatch in  $P_t(A)$  function, which is compatible with the current sheet identification approach of looking for abrupt changes in the same time series measurements. Of course, we acknowledge that we may miss some, especially in relatively large scales. Nonetheless, we believe that we have provided the direct evidence, through our unique approach, in supporting the view of locally generated coherent structures intrinsic to the dynamic processes in the solar wind as manifested either by magnetic reconnection or inverse turbulence cascade.

Furthermore, with the small-scale flux rope database derived via the unique GS method, it is easy to further derive the axial current density distribution inside

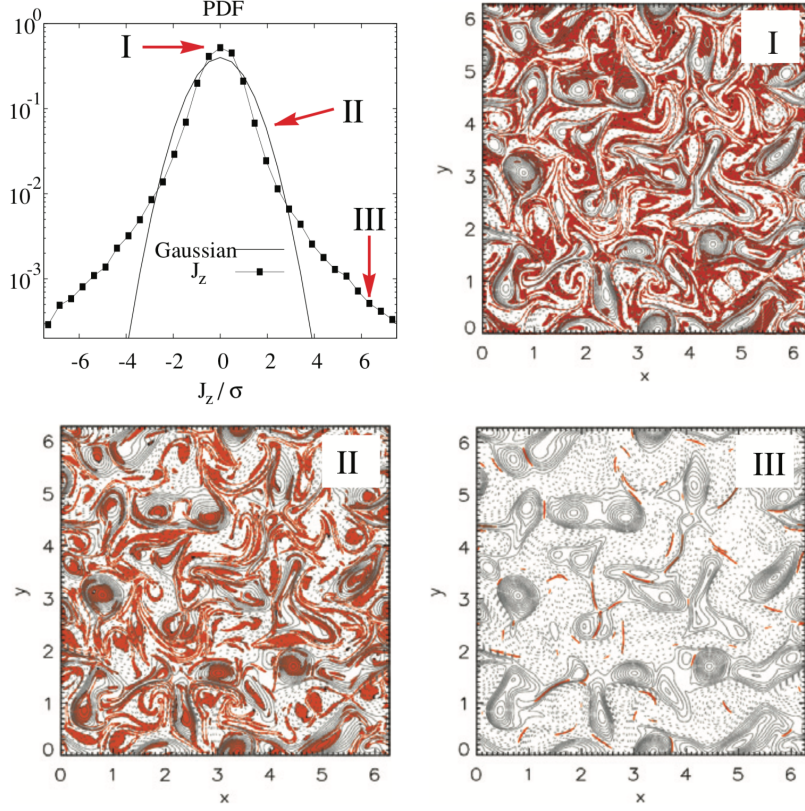


**Figure 4.18:** PDF of the out-of-plane electric current density  $J_z$  from the 2-D simulation, compared to a reference standard Gaussian distribution. The colored (red) regions in subfigures I, II, and III are places where the selected band (I, II, or III) corresponds to. Region I: very low values of fluctuations that lie mainly in the lanes between magnetic islands. Region II: current cores of central regions of magnetic islands. Region III: small-scale current sheet-like structures that form the sharp boundaries between the magnetic islands. (Credit: Greco et al. [97]).

the small-scale flux ropes, and to compare with numerical simulation result. From Chapter 2, the derivative of the total transverse pressure  $P_t$  with respect to the flux function  $A$  is just the current density along the flux rope axial direction  $J_z$ . Figure 4.17 is the histogram of the axial current density inside the small-scale flux ropes derived from our database. It is generated by sampling each flux rope interval to get the  $J_z$  distribution. Because of the different sizes of these flux ropes, we make

the sampling rate proportional to the flux rope scale sizes, in order to make the sampled points distributed uniformly in space. The  $J_z$  values of the black curves marked by dots, squares, and triangles are normalized by  $\sigma$ ,  $2\sigma$ , or  $3\sigma$ , respectively, where  $\sigma$  represents the standard deviation of  $J_z$  from our database. Figure 4.18 shows the PDF of the out-of-plane current density  $J_z$  from the 2-D simulation by Greco et al. [97]. This PDF is contributed by currents from three regions shown in subfigures I, II, and III. Comparing Figure 4.17 to Figure 4.18, one can see that the distribution of  $J_z$  normalized by  $1\sigma$  in Figure 4.17 is similar to the  $J_z$  distribution in Figure 4.18. However, this direct comparison is not appropriate. In Figure 4.17, the  $J_z$  distribution is only contributed by the current density within small-scale flux ropes, corresponding to region I and region II in Figure 4.18. Due to the lack of large  $J_z$  values (corresponding to region III), the standard deviation  $\sigma$  of  $J_z$  in Figure 4.17 must be smaller than that in Figure 4.18. To make the normalized curves in Figure 4.17 and Figure 4.18 comparable, we use larger values, i.e.,  $2\sigma$  and  $3\sigma$ , to normalize  $J_z$  values in Figure 4.17, which are shown by squares and triangles, respectively. From these two curves, one can see that there is lacking of relatively strong current densities in Figure 4.17. This is consistent with the fact that there are no elongated structures contributing to our  $J_z$  data set, compared to Region II and III in Figure 4.18.

This comparison shows that we get the similar  $J_z$  distribution via a totally different method while validating Greco et al.'s result. This is largely owing to the unique capability of the GS method in deriving the current density distributions from time-series single-spacecraft measurements.

## 4.5 Locations of Small-scale Magnetic Flux Ropes with Respect to the Heliospheric Current Sheet (HCS)

The argument that the small-scale flux ropes are created locally is in part based on the fact that some events were found near the heliospheric current sheet (HCS). Upon the first discovery of small-scale flux ropes, Moldwin et al. [52] interpreted their findings in terms of multiple magnetic reconnection of previously open field lines at the HCS [52]. Later, Moldwin et al. [53] reported several additional small-scale flux ropes observed by both IMP 8 and/or Wind spacecraft. They suggested that these small-scale flux ropes were created in the HCS instead of the solar corona because of the following reasons: (1) bimodal size distribution, (2) lack of expansion, (3) different plasma characteristics, and (4) similar radial scale size with estimated HCS thickness. Cartwright and Moldwin [72] studied the distribution of small-scale flux ropes with respect to the HCSs, and found that most events were observed near HCSs, although, as we pointed out earlier, their event samples are extremely small. In this section, we redo the same analysis based on our database, which contains much more number of events than Cartwright and Moldwin's dataset.

Figure 4.19 is the histogram of the time to the nearest HCS for the small-scale flux ropes in our database. The HCS crossing times are taken from L. Svalgaard's list of sector boundaries in the solar wind (<http://www.leif.org/research/sblist.txt>). This plot indicates that the small-scale flux ropes tend to appear near the sector crossings. This result is consistent with Cartwright and Moldwin's result (see Figure 9 in their paper [72]). However, from Figure 4.19 one can see that the peak of the black curve

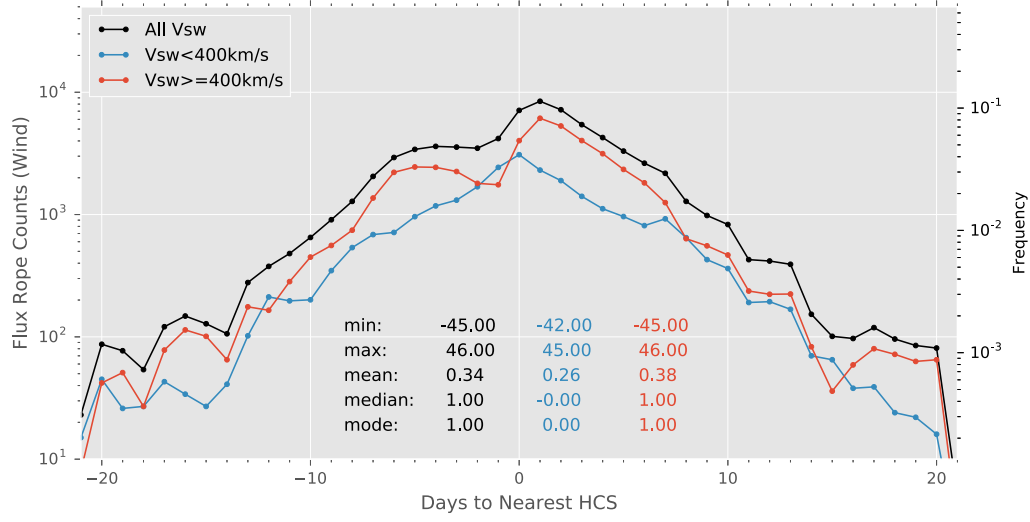


**Figure 4.19:** Small-scale flux rope distribution with respect to the time to the nearest heliospheric current sheet. The events are binned by 1 day. Negative value means the time ahead of the HCS. The red and blue curves represent the events occurring under different solar wind speed conditions (blue curve:  $\bar{V}_{sw} < 400$  km/s, red curve:  $\bar{V}_{sw} \geq 400$  km/s).

is located at 1 day after the HCS crossings, instead of 0 day shown in Cartwright and Moldwin's result [72]. After we split the entire event set into two subsets based on solar wind speed, we find that the events with solar wind speed less than 400 km/s tend to occur within 1 day with respect to HCSs with a central peak right at 0 day. The events with solar wind speed greater than or equal to 400 km/s tend to occur at 1 day after HCSs, with two broad and asymmetric peaks at  $\sim -5$  days and  $\sim 1$  day. Correspondingly, a broad secondary peak is also located at  $-5$  days for the black curve. The similar trend of black and red curves ( $\bar{V}_{sw} > 400$  km/s) implies that the secondary peak in the black curve is contributed by the events with solar wind speed  $\bar{V}_{sw} \geq 400$  km/s. The peak at  $\sim 1$  day is more pronounced, indicating a close association to HCS crossings for relatively fast solar wind. We caution not to over-

interpret the peak preceding the HCS crossings, which is weak and the separation is large so that the association is much less certain. We offer an alternative explanation which is that the flux ropes near  $-5$  day to HCSs possibly occur right after other HCSs, but these HCSs are not observed due to unknown reasons. As a result, these flux ropes appear to occur at a relatively larger separation time preceding the nearest HCSs. This can happen when the sector boundaries are not in the ecliptic plane, so that they are not observed by the spacecraft in the ecliptic plane. The blue curve ( $\bar{V}_{sw} < 400$  km/s) is symmetric, which is different from the red curve. The peak of the blue curve is at 0 day, indicating that the small-scale flux ropes tend to occur in the same day with HCS crossings under slow solar wind speed condition.

In order to look into more details on the distribution of flux rope occurrence time with respect to HCSs, we plot the histograms of days to nearest HCSs for each year in Figure 4.20. From Figure 4.20, one can see that the small-scale flux ropes do appear near HCSs in each year, although the spread in time can be wide, reaching  $\pm 10$  days. In addition, the distributions have year by year variations. During solar cycle 23 (1996~2008), the histograms show a triangle distribution in the years 1998, 1999, 2000, and 2001, all of which are during ascending phase of solar activity. The histograms show an additional peak near  $-5$  days in the years 2002, 2003, and 2004, all of which are during the descending phase. However, in solar cycle 24, there is no such a clear classification. The double peaks show up in years 2011, 2013, 2014, and 2016, in which 2011 and 2013 are during the ascending phase, while 2014 and 2016 are during the descending phase. From the analysis on Figure 4.19, we conclude that the secondary peaks near  $-5$  day are more directly associated with medium and

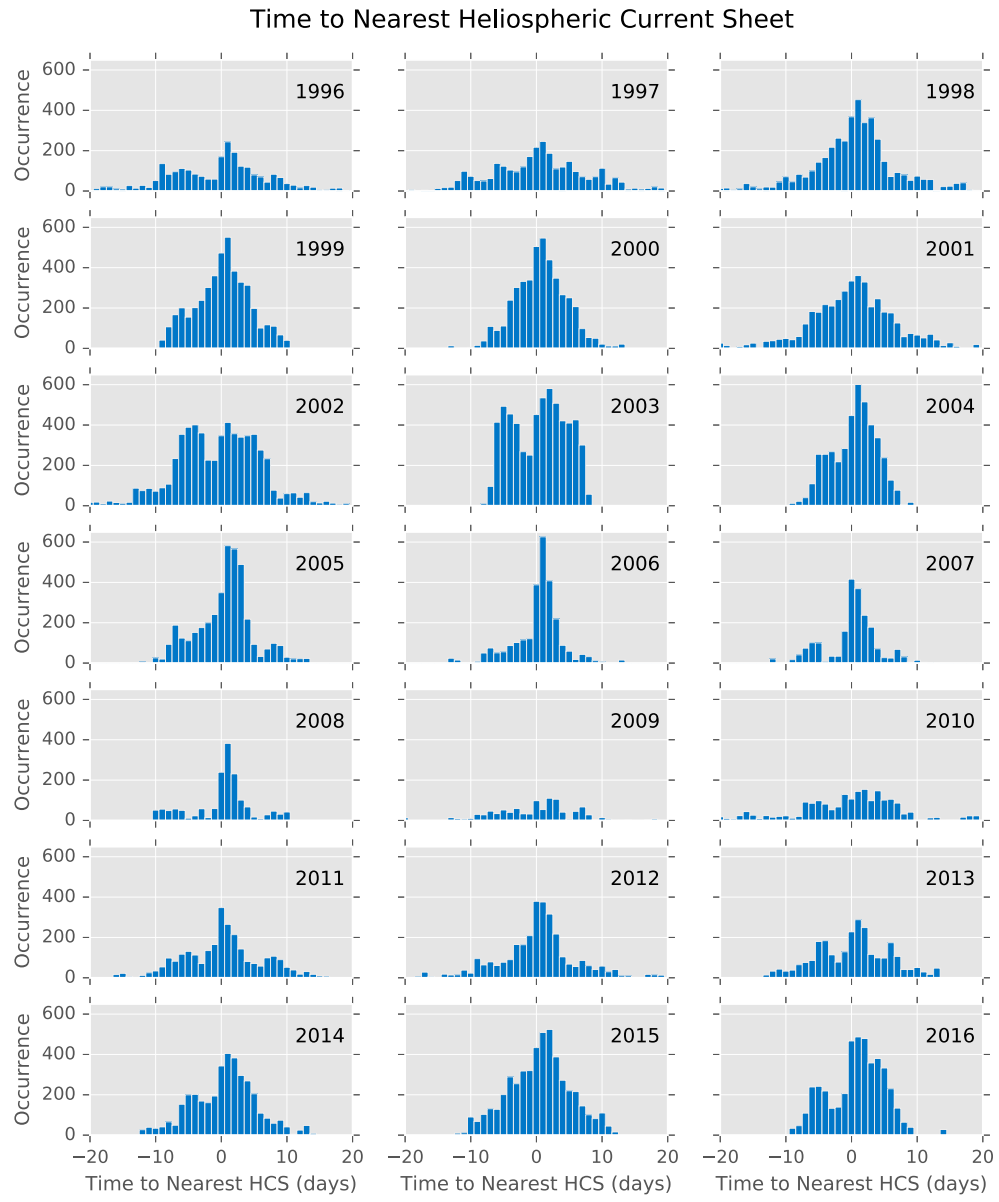
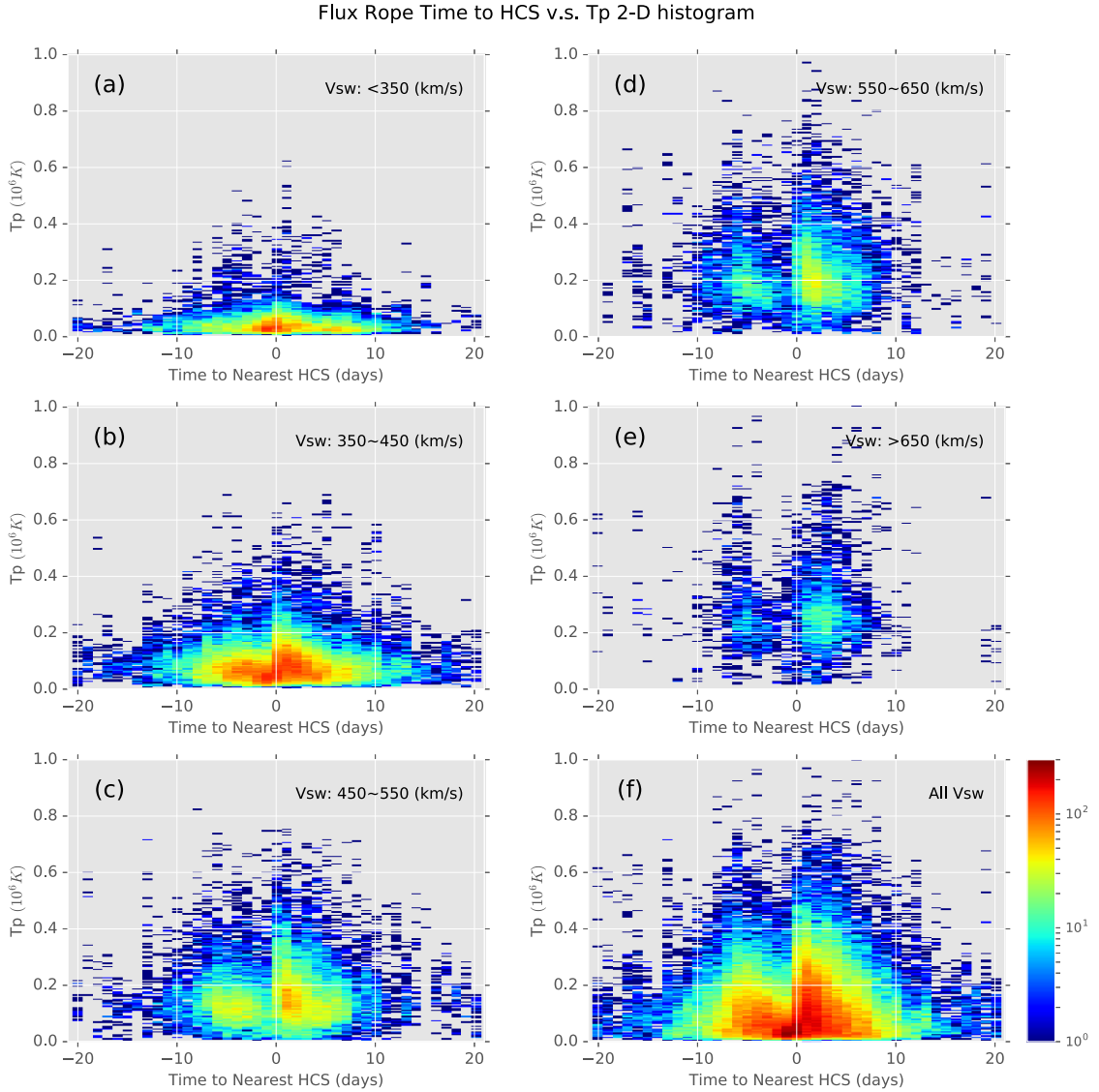


**Figure 4.20:** Annual small-scale flux rope counts distribution with respect to the nearest heliospheric current sheet. The events are binned by 1 day. Negative days mean the occurrence time ahead of HCS.

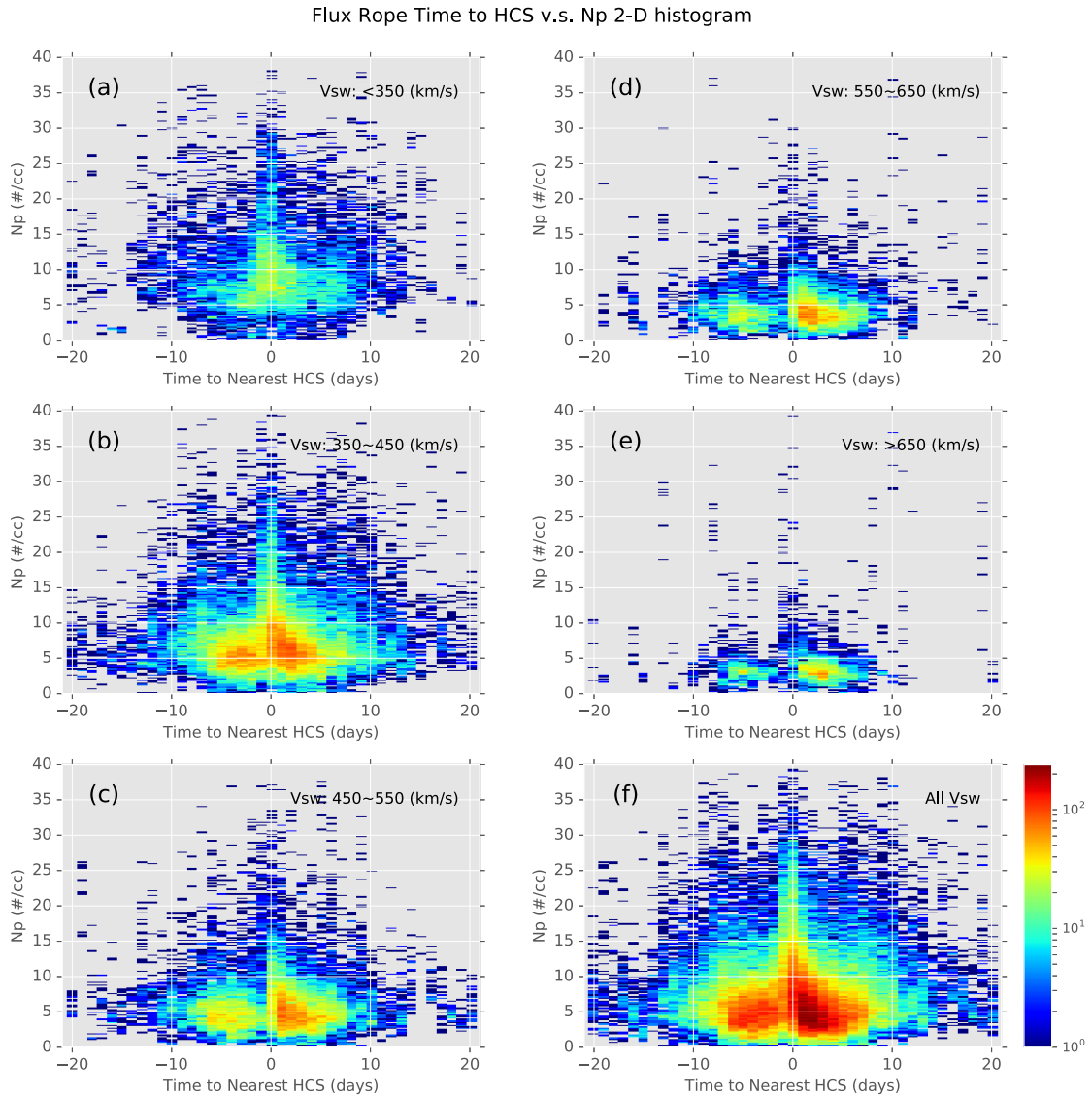
high speed solar wind. In Figure 4.20, most of those years that have secondary peaks are during the descending phases of each solar cycle, which are usually dominated by high speed solar wind streams.

Figure 4.21 and Figure 4.22 are the 2-D histograms of time to the nearest HCS *versus* average proton temperature and average proton number density, respectively. Figure 4.21 (a) and (b) show that the small-scale flux ropes with lower proton temperature spread widely around the HCSs. Figure 4.21 (c), (d), and (e) show that in medium and high speed solar wind, there are less number of small-scale flux ropes appearing far from HCSs, and the proton temperature is elevated. The triangle outline in Figure 4.21 (f) shows a pattern consistent with Figure 4.19. Each panel of Figure 4.22 shows that the flux ropes with higher proton number density are more likely to appear near the HCSs. We also note the location of the colors denoting higher occurrence rate (red color and yellow color). In Figure 4.22 (a), the yellow color region is within the range  $5 \leq N_p \leq 15$ . In Figure 4.22 (b), the upper boundary of the red and yellow color region is at about  $N_p = 15$ , but the lower boundary goes below  $N_p = 5$ . In Figure 4.22 (c) and (d) the red and yellow color region moves down to  $0 \leq N_p \leq 10$ , and in Figure 4.22 (e), the red and yellow color region is below  $N_p = 5$ . The different locations of the red and yellow color regions in different solar wind speed indicate that in higher solar wind speed streams, the flux ropes tend to have lower proton number density.

Combining Figure 4.21 and Figure 4.22, we conclude that small-scale flux ropes occurring at the HCS crossings (0 day) tend to have lower average proton temperature and higher average density, consistent with the general plasma property of the HCS,



**Figure 4.21:** The 2-D histograms of flux rope average proton temperature *versus* time to the nearest HCS. The *x*-aixs is binned by 1 day. Negative values mean the time ahead of HCS. Subplots (a) to (e) are histograms under different solar wind speeds, and subplot (f) is the histogram for the entire dataset. The color bar represents the small-scale flux rope counts.



**Figure 4.22:** The 2-D histograms of flux rope average proton number density *versus* time to the nearest HCS. The format is the same as in Figure 4.21.

embedded in low speed streams. The opposite seems to be the case for flux ropes occurring in the vicinity of HCS, within  $\pm 10$  days.

## CHAPTER 5

### ASSOCIATION BETWEEN SMALL-SCALE MAGNETIC FLUX ROPES AND INTERPLANETARY SHOCKS

#### 5.1 Introduction

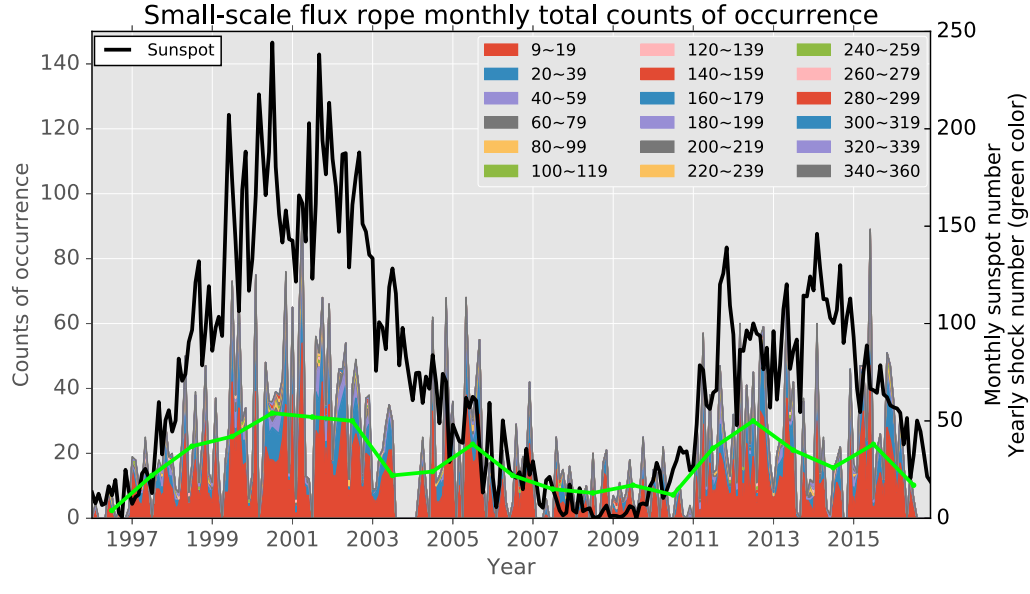
Interplanetary shocks are known sources contributing to energetic particle acceleration and transport in the heliosphere. However observations show that in certain energy ranges particle behavior deviates from expected shock related acceleration processes. The association between structures (mainly discontinuities) other than shocks and local energetic particle flux enhancements were also reported by a number of studies [83, 84, 90, 96, 100, 101]. Theoretical investigations suggested that the combination of diffusive shock acceleration and downstream multiple magnetic island acceleration would result in the energization of charged particles [81, 93]. We have found observational evidence of flux rope structures downstream of shocks (see also Chapter 2) and of possible local particle energization [94]. In this chapter, we follow up with further analysis of the occurrence and properties of flux ropes downstream of shocks and the associated energetic particle signatures. In particular, we are going to present two sets of case studies in which the enhanced ions flux was observed within the flux rope region. We will use the combined observations of ACE and Wind spacecraft to

illustrate the change in flux rope morphology especially in terms of merging process leading to particle energization.

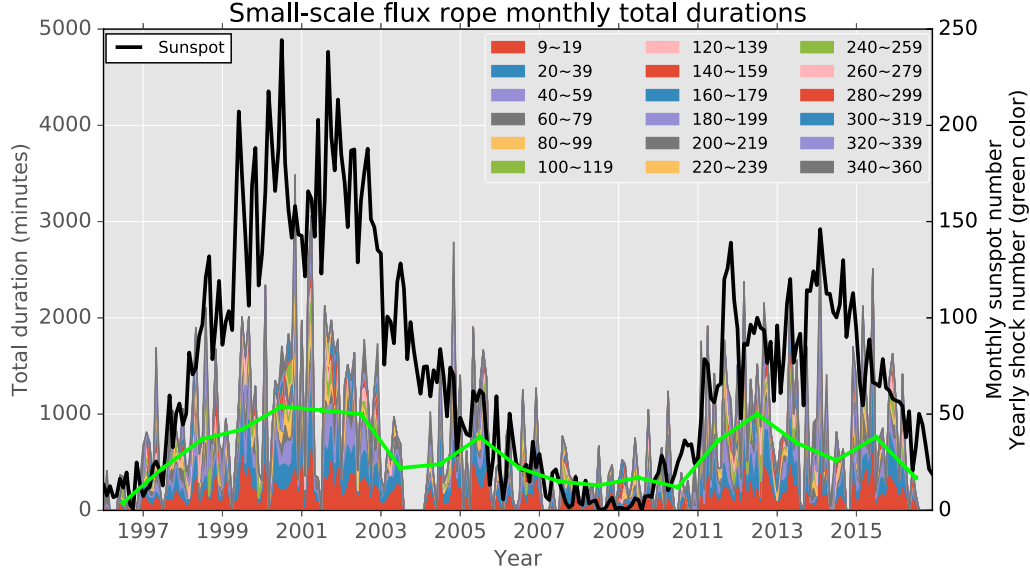
Our analysis employs existing online resources such as databases containing identified shock waves and other types of discontinuities or structures. For example, they include, but are not limited to, the online shock database from the ACE spacecraft at Earth, and the similar but more comprehensive Heliospheric Shock Database (<http://ipshocks.fi/>) that lists identified shock waves from multiple spacecraft in the solar wind. The associated shock parameters such as the geometry of the shock, the shock speed, and compression ratios etc. are also given in these databases.

In this section, we perform some basic analysis on small-scale flux ropes found downstream of shocks, in order to find the aspects that distinguish them from the entire set of events. We aim to address these questions: (1) are these flux ropes generated by shocks, (2) is their creation independent of shocks but are their properties affected by shocks, and (3) how are they related to energetic particles? We will first repeat some statistical analysis as what we have done on the entire event set in Chapter 4, then we will perform case studies to investigate in detail the characteristics of the small-scale flux ropes downstream the shock.

Figure 5.1 (a) and (b) are the monthly occurrence counts and total duration of small-scale flux ropes identified downstream of shocks, in the same format as in Figure 4.1 (a) and (b). Comparing Figure 5.1 with Figure 4.1, one can see that the occurrence counts show a similar trend, indicating that flux ropes downstream of shocks have the same solar cycle dependency as the general flux rope population. When we look into the details, we find that there is a difference between Figure 5.1

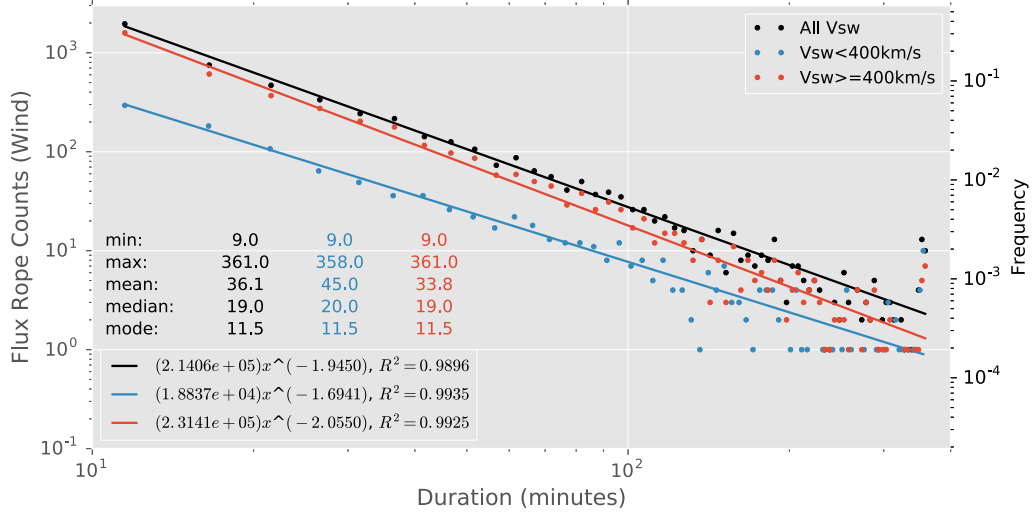


(a)

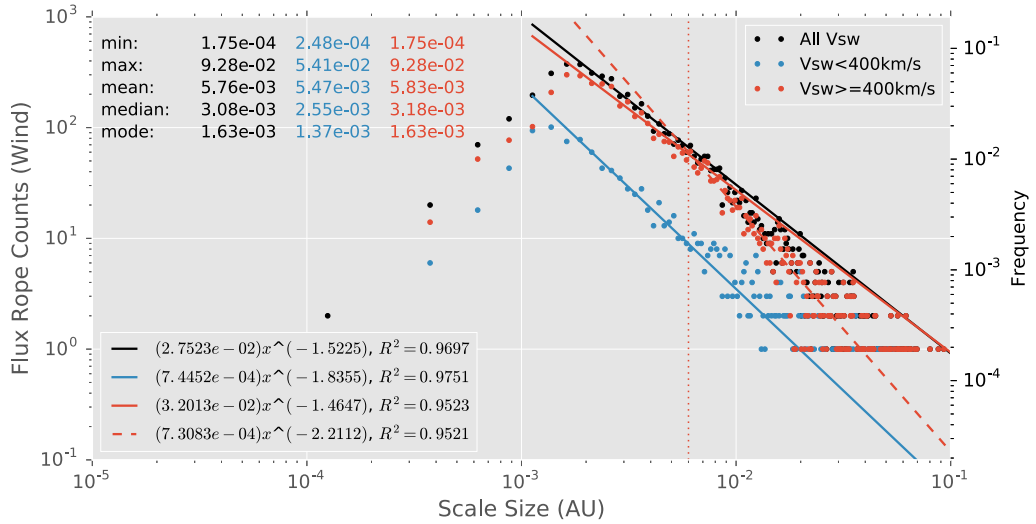


(b)

**Figure 5.1:** (a) The monthly counts of flux rope events occurrence (left axis) and the monthly sunspot numbers (black curve; right axis) during 1996-2016. Colors represent counts of events with different durations as indicated. Green solid curve shows the yearly shock number observed by Wind spacecraft. (b) The monthly flux rope total duration (left axis) and the monthly sunspot numbers (right axis) during 1996-2016. The format is the same as in (a). For both (a) and (b), all the flux ropes are downstream of shocks (within 12 hours downstream from the shock time).



(a)



(b)

**Figure 5.2:** (a) The histogram of small-scale flux rope duration plotted in logarithmic scales. The time range is from 9 minutes to 361 minutes, with 5 minutes bin size. (b) The histogram of small-scale flux rope cross section scale sizes plotted in logarithmic scales, with 0.00025 AU bin size. The flux rope scale size is calculated from the flux rope duration taking into account the axial orientation. For both (a) and (b), the basic statistical and linear regression parameters for each curve are listed, respectively. The format is the same as in Figure 4.9. The only difference is that, in this plot, all the flux ropes are downstream of shocks (within the 12-hour interval after the shock time).

(a) and Figure 4.1 (a). The occurrence peak appears near year 2003 in Figure 4.1 (a), while in Figure 5.1 (a), the occurrence peak is located near year 2001, and instead of a peak, there is a big gap in year 2004. Since these events are picked downstream of shocks, the shock occurrence rate will affect the flux ropes occurrence rate. To see the effect of shock occurrence on the flux ropes occurrence, we plot the yearly counts of shocks observed by the Wind spacecraft. The green curve in Figure 5.1 (a) shows the trend of shock occurrence from 1996 to 2016 (also shown in Figure 5.1 (b)). We find that the flux rope occurrence trend in Figure 5.1 (a) follows the trend of shock occurrence counts better than the trend of the sunspot numbers shown in Figure 5.1 (a). It seems that the minor difference of the occurrence trend between Figure 5.1 (a) and Figure 4.1 (a) is due to the modulation of the shock occurrence. So the flux ropes downstream of shocks are just a subset of the entire flux rope database. They are selected within the interval starting from the shock time and ending at 12 hours after the shock time which is chosen by considering the range of shock effect.

Figure 5.2 (a) and (b) are the corresponding distribution of duration and scale size, respectively, for the flux ropes downstream of shocks. The format of Figure 5.2 is the same as in Figure 4.9, as well as the fittings. Comparing Figure 5.2 (a) with Figure 4.9 (a), we find that, under each solar wind speed condition, the power law index of the fitted curve is similar to its counterpart in Figure 5.2 (a). The difference is that, in Figure 5.2 (a), the flux ropes in medium and high speed solar wind dominate over the whole ranges of duration and scale size. This is expected since the shocks are usually associated with high speed solar wind. Similar results are obtained by comparing Figure 5.2 (b) and Figure 4.9 (b).

Combining the analyses on Figure 5.1 and Figure 5.2, we speculate that flux ropes downstream of shocks are just a subset of the entire flux rope database. Except for the modulation of occurrence, the shocks appear to have little effect on the small-scale flux rope distributions. We also have further compared other statistical properties, such as flux rope orientations, waiting time distributions of the two different kinds, and the wall-to-wall time. We do not observe any obvious difference which could distinguish the flux ropes downstream of shocks from the entire small-scale flux rope database. This preliminary analysis suggests that these flux ropes downstream of shocks may not be generated by shocks. It is also not clear whether shocks can significantly enhance or modify flux ropes downstream, except for some properties of the flux ropes such as the temperature and density, intrinsic to the enhancement downstream of shocks.

## 5.2 Case Studies

We present two case studies with the radial alignment of the ACE and Wind spacecraft in the solar wind. One event involves a shock that was observed by ACE on March 10th, 1999, at 00:40 UT, and observed again by Wind about 53 minutes later. The other event has a shock that was observed by ACE on December 7th, 2003, at 13:41 UT, but not observed by Wind. The downstream streams passed the two spacecraft in both events. We examine the magnetic field, solar wind plasma, and energetic ions data beginning from 1 hour upstream the shock and ending at 9 hours downstream each shock. In each ten-hour interval, a few flux ropes are detected, and

the combined observations of ACE and Wind suggest flux rope merging in the region of enhanced energetic ion flux.

### 5.2.1 CASE 1: 1999/3/9 23:40 UT $\sim$ 1999/3/10 09:40 UT

Figure 5.3 and Figure 5.4 show time series data around the same shock observed by ACE and Wind successively. Figure 5.3 shows a shock observed at 00:40 UT at ACE, while in Figure 5.4, the shock time is 01:33 UT. The two observations are 53 minutes apart. In Figure 5.3, we note that during the intervals of flux ropes No.7 and No.8, the ions flux is enhanced  $\sim$  5 hours downstream of the shock. Within the interval of flux rope No.7, the ions flux is enhanced by 5 times in the  $0.068 \sim 0.115$  MeV channel and by 3 times in the  $0.047 \sim 0.068$  MeV channel. In each case, the enhancement peak is near the center of the flux rope interval. Panels five and six show that after the shock passage, there is a weak ion flux enhancement from 01:00 UT to 02:00 UT, and after 02:00 UT, the ion flux level returns to the background value. Thereafter, starting at about 05:30 UT, the ion flux reaches two consecutive peaks. We believe that these two ion flux peaks are less likely caused by direct shock acceleration. Instead, they may be caused by other co-located structure or processes, such as flux rope merging or contraction. Noting that these two flux ropes are next to each other, which makes the interaction with each other possible. If they are merging, we should be able to see one single flux rope after some time. In order to check their temporal evolution, we examine the flux rope events observed by Wind which is radially aligned with ACE at a distance  $\sim$  247 Earth radii further upstream toward Earth. We try to find the correspondence to flux ropes No.7 and No.8 in Figure 5.3.

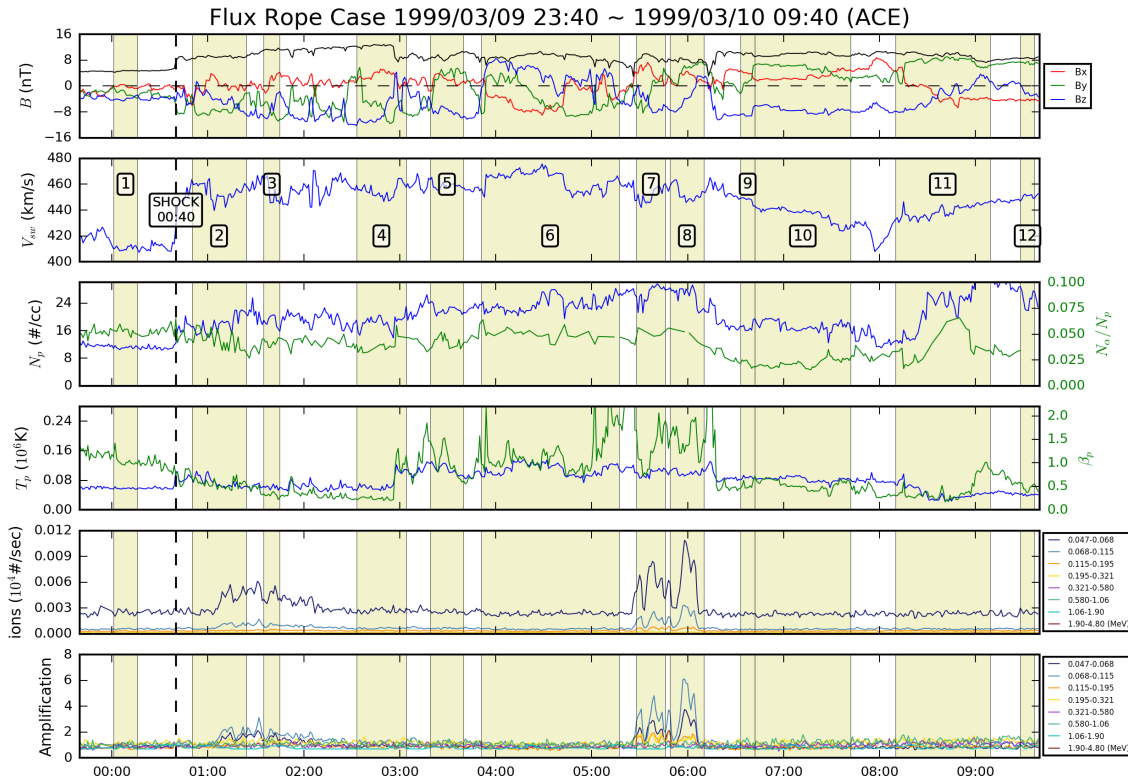


**Figure 5.3:** Time series data from March 9th, 1999, 23:40 UT to March 10th, 1999, 09:40 UT. All data are from the ACE spacecraft. This time interval contains one interplanetary shock and twelve identified flux rope structures which are labeled from 1 to 12 as marked and shaded by yellow color. The first panel is the magnetic field data in the GSE coordinates. The black solid line denotes the total magnetic field magnitude. The second panel is the solar wind bulk speed. In the third panel, the proton number density is shown in blue and the alpha/proton number density ratio is shown in green. The fourth panel are the proton temperature (in blue line) and proton plasma beta (in green line). The fifth panel is ions flux, and the sixth panel shows the same ions flux, but normalized by the value at shock time. The energy range of each curve is provided in the box to the right. They correspond to the following energy channels of the EPAM instruments: 0.047  $\sim$  0.068 MeV, 0.068  $\sim$  0.115 MeV, 0.115  $\sim$  0.195 MeV, 0.195  $\sim$  0.321 MeV, 0.321  $\sim$  0.580 MeV, 0.580  $\sim$  1.06 MeV, 1.06  $\sim$  1.90 MeV, and 1.90  $\sim$  4.80 MeV. The shock is denoted by a vertical black dashed line across all panels.

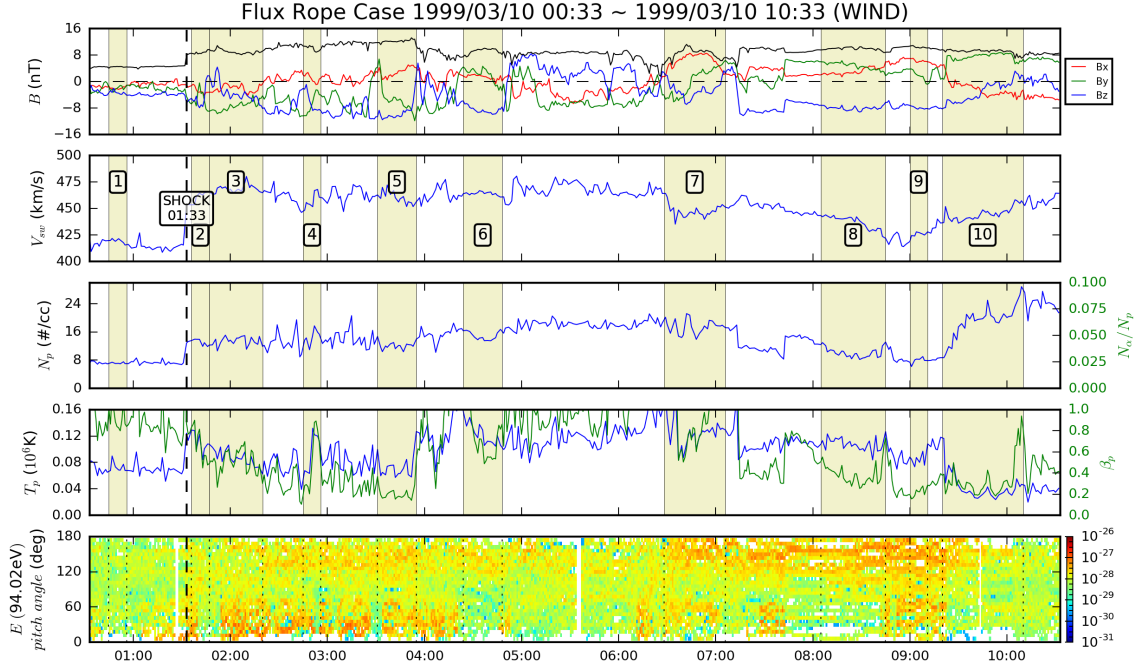


**Figure 5.4:** Time series data from March 10th, 1999, 00:33 UT to March 10th, 1999, 10:33 UT. All data are from the Wind spacecraft. This time interval contains one interplanetary shock and ten flux rope structures which are labeled from 1 to 10 and shaded by yellow color. The top four panels are in the same format as Figure 5.3. The fifth panel shows suprathermal electron pitch angle distribution. The shock is denoted by a vertical black dashed line across all panels.

From Figure 5.4, we can see that the Wind flux rope No.7 has similar magnetic field structure to the combined intervals of ACE flux ropes No.7 and No.8 in Figure 5.3. Also, their neighboring magnetic field structures are highly similar as separated by current-sheet type boundaries. We believe that the Wind flux rope No.7 can be identified as the correspondence to ACE flux ropes No.7 and No.8. To verify our speculation, we check the time shift between ACE and Wind flux ropes, and compare it with propagating time of solar wind. Figure 5.5 shows the positions of ACE (red triangle), Wind (green triangle) spacecraft, and the Earth (blue dot) in

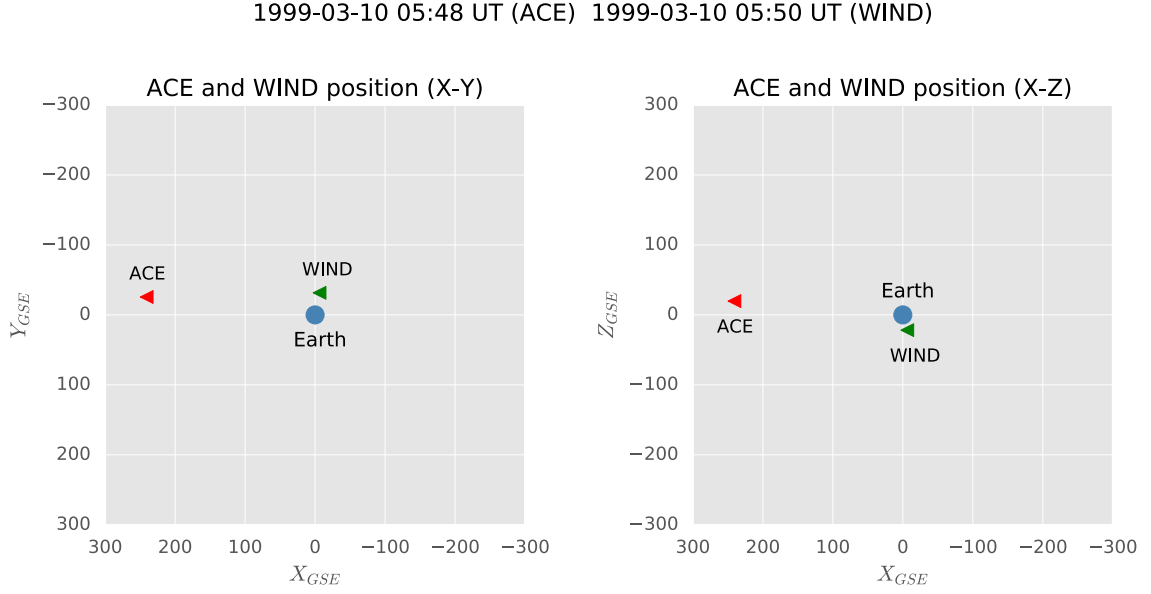
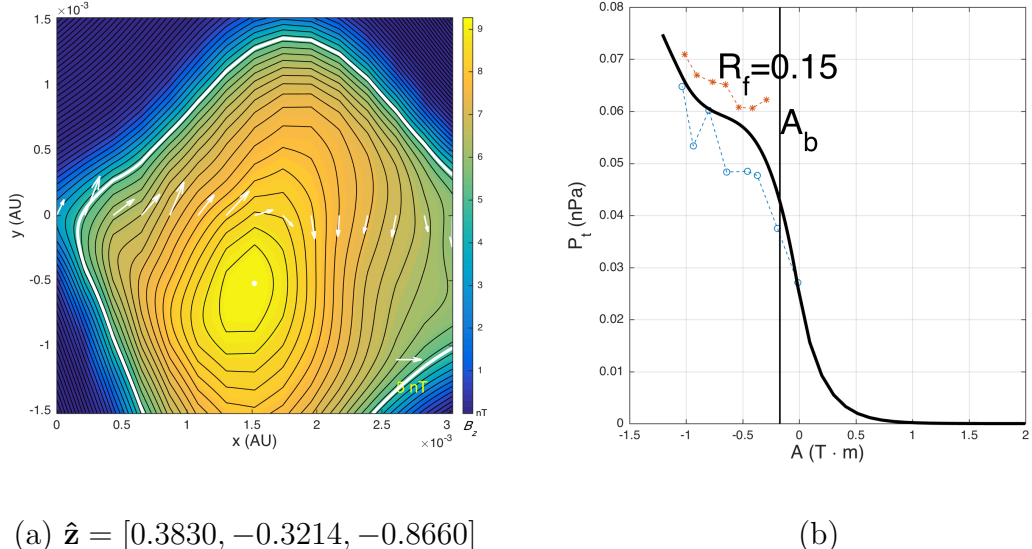


**Figure 5.5:** The positions of ACE and Wind spacecraft in the GSE coordinates. The left panel is the projection on XY-plane, and the right panel is the projection on XZ-plane. The time stamp of ACE is March 10th, 1999, 5:48 UT, and the time stamp of Wind is March 10th, 1999, 5:50 UT. The unit of all axes is Earth radius.

the GSE coordinates when ACE was in the center of flux rope No.7 in Figure 5.3 (at about 05:48 UT). Since the flux rope propagating time is less than 2 hours, in such a short time, we can assume that both spacecraft are stationary. We can see that the ACE and Wind are aligned along  $X_{GSE}$  axis, and ACE is ahead of Wind in the direction toward the Sun. The GSE coordinates of ACE are  $(X, Y, Z) = (1.53359 \times 10^6, -1.63047 \times 10^5, 1.25898 \times 10^5)$  km, and the GSE coordinates of Wind are  $(X, Y, Z) = (-4.0486 \times 10^4, -2.0099 \times 10^5, -1.3872 \times 10^5)$  km. From their coordinates, we can calculate the separation between ACE and Wind in the  $X_{GSE}$  direction which is  $1.57408 \times 10^6$  km. From the second panels of Figure 5.3 and Figure 5.4, we can obtain the average solar wind speed during the flux rope intervals under consideration (No.7

and No.8 in Figure 5.3, and No.7 in Figure 5.4) which is about 450 km/s. Therefore, the propagating time for a flux rope from ACE to Wind is about 58 minutes. Then we are going to check the time shift of flux ropes No.7 and No.8 in Figure 5.3, and the flux rope No.7 in Figure 5.4. The center time of flux ropes No.7 and No.8 in Figure 5.3 is 05:49 UT (the center between the start time of flux rope No.7 and the end time of flux rope No.8), while the center time of flux rope No.7 in Figure 5.4 is 06:47 UT. The time shift is 58 minutes, which is the same as the calculated propagating time. Now we are confident that the flux rope observed by Wind is a later evolution phase of the flux ropes No.7 and No.8 observed by ACE.

In order to show the flux rope evolution from ACE to Wind, we reconstruct the flux ropes No.7 and No.8 in Figure 5.3, and the flux rope No.7 in Figure 5.4 by the GS reconstruction method. Figure 5.6 (a) shows the reconstructed cross section of flux rope No.7 in Figure 5.3. The white arrows are the transverse field vectors along the projection of the spacecraft path on the  $x$ - $y$  plane. The color represents the  $B_z$  field of this flux rope with scales given by the colorbar. The arrow directions indicate that this flux rope has the left-handed chirality. The maximum  $B_z$  field is about 9 nT in the flux rope center. Figure 5.6 (b) is the fitting curve of  $P_t(A)$ , in which  $P_t$  is the transverse plasma pressure, the sum of plasma and axial magnetic pressure, and  $A$  is the magnetic flux function. Though the fitting residue  $R_f$  is acceptable, the two branches of measured data points (in red and blue, respectively) still have notable deviations, which indicates that the current axial orientation we found may not be the optimal one. We will discuss it later when we analyze the axial orientations. Figure 5.7 (a) is the reconstructed cross section of the flux rope No.8 in Figure 5.3,



(a)  $\hat{\mathbf{z}} = [0.3830, -0.3214, -0.8660]$

(b)

**Figure 5.6:** GS reconstruction result for flux rope record No.7 (March 9th, 1999, 05:28 - 05:46 UT) in Figure 5.3. (a) The cross-section magnetic field configuration of the flux rope. The unit vector  $\hat{\mathbf{z}}$  represents the  $z$  axis orientation of the flux rope. The filled color contour represents the axial magnetic field  $B_z$  and the line contour overlapped in black represents the transverse magnetic field. The white arrows across the map horizontally are projected transverse magnetic field vectors along the spacecraft path. The white contour line encloses the region  $A < A_b$  in this case (within the flux rope boundary  $A = A_b$ , denoted in (b)). The reconstruction map within this line is reconstructed by the double-folded spacecraft data, and the region beyond this line is reconstructed based on the extrapolated data. (b) The fitting curve (bold solid line) of  $P_t(A)$  for this flux rope case. The fitting is based on the data points denoted by blue circles and red stars, where the circles represent the data sampled as the spacecraft crossed the first half of the flux rope structure and the stars represent those of the second half. The thin vertical solid line denoted by  $A_b$  marks the boundary corresponding to the white line in (a). A fitting residue  $R_f$  is also denoted.

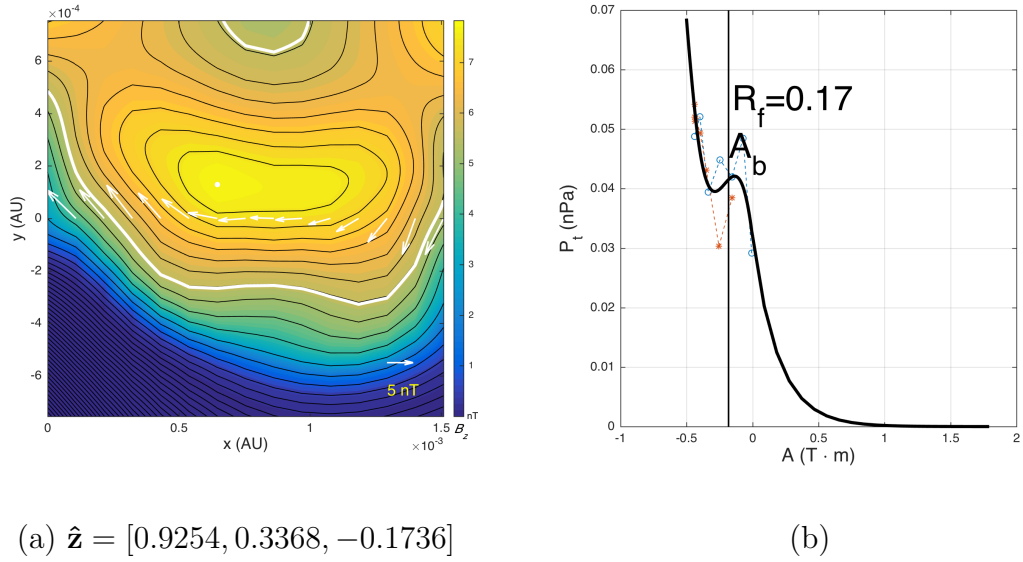


**Figure 5.7:** GS reconstruction result for flux rope record No.8 (March 9th, 1999, 05:49 - 06:10 UT) in Figure 5.3. The format is the same as Figure 5.6.

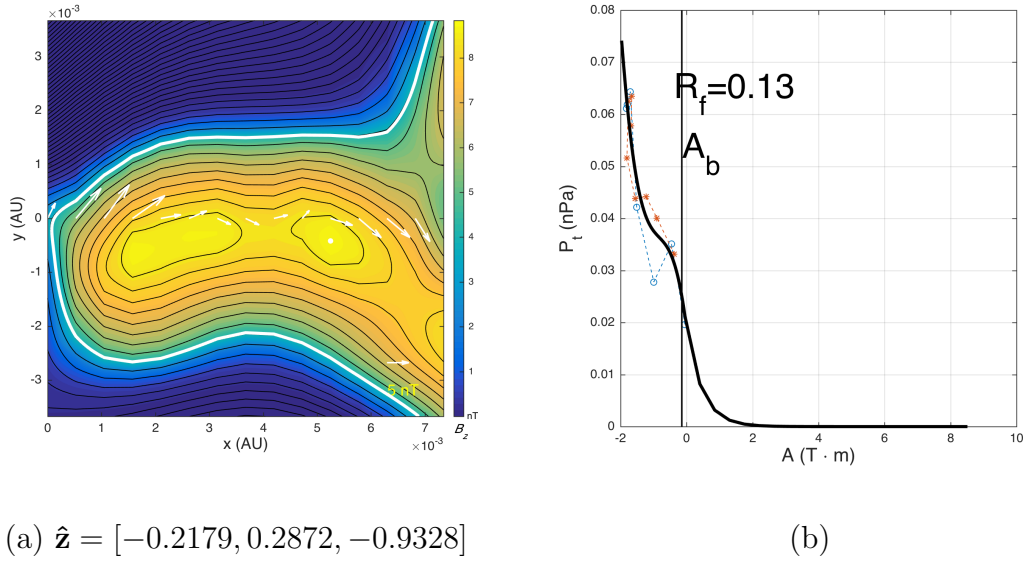
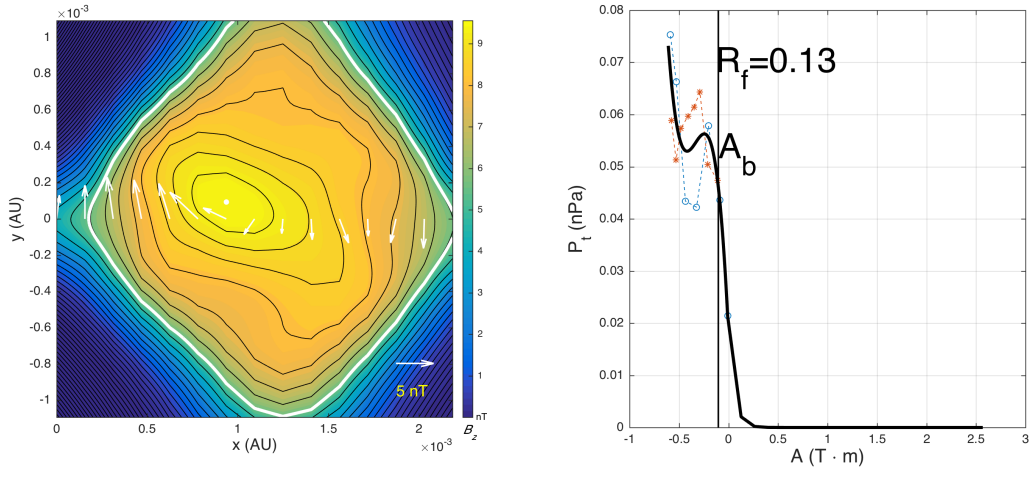


**Figure 5.8:** GS reconstruction result for the combination of flux ropes No.7 and No.8 (March 9th, 1999, 05:28 - 06:10 UT) in Figure 5.3. The format is the same as Figure 5.6.

which is next to flux rope No.7. Its maximum  $B_z$  field is about 8.5 nT, which is relatively weaker than its neighbor. No.8 has the same left-handed chirality as No.7. Their  $\hat{\mathbf{z}}$  axis orientations differ by  $67^\circ$ . Two neighboring flux ropes with the same chirality and interacting with an oblique and acute angle between their cylindrical axes may merge due to magnetic reconnection [155].

Since No.7 and No.8 are close to each other, we tried to put these two flux rope intervals together to see if we can find the combined structure, i.e., possible configuration of double flux ropes. The same approach had been successfully applied to large-scale multiple flux ropes in the solar wind [115]. Figure 5.8 (a) is the reconstructed cross section when we perform GS reconstruction on the entire interval combining No.7 and No.8 together. A twin flux rope shape cross section is obtained. The fitting residue shown in Figure 5.8 (b) is smaller than both of the individual ones in Figure 5.6 (b) and Figure 5.7 (b). When checking the axial orientation of each individual flux rope and comparing them with the combined flux rope, we find that they have three different axial orientations. This means that the structures of flux rope No.7 and No.8 are not strictly 2-D structures. This is also partially the reason why the two individually reconstructed flux ropes do not have very small fitting residues.

Figure 5.9 (a) is the reconstructed cross section of flux rope No.7 in Figure 5.4. This flux rope is observed by Wind and is the counterpart of the combined flux ropes No.7 and No.8 observed by ACE in Figure 5.3. It has similar core field strength but smaller size compared with the combined flux rope observed by ACE. From Figure 5.8 (a) to Figure 5.9 (a), we see the process that the twin flux rope structure merges into



(a)  $\hat{\mathbf{z}} = [0.9397, 0.0000, -0.34207]$

(b)

**Figure 5.9:** GS reconstruction result for the flux rope record No.7 (March 9th, 1999, 05:49 - 06:10 UT) in Figure 5.4. The format is the same as Figure 5.6.

a single one, although each is shown as a snapshot at the specific time, respectively.

The irregular transverse field lines in Figure 5.9 (a) implies that this flux rope just underwent a non-steady evolution process. It is interesting to note that the axial orientation of the Wind flux rope is also different from the combined flux rope from ACE. The angle between their axial orientations is  $83^\circ$ . This shows that the flux rope orientation is subject to change in the merging or propagating process, either due to the overall rotation or the more complicated 3-D effect generated in the merging process [155].

### 5.2.2 CASE 2: 2003/12/7 12:41 UT ~ 2003/12/7 22:41 UT

In this case study, another ion flux enhancement event during a flux rope interval is observed, and the radial evolution of the corresponding flux rope is analyzed

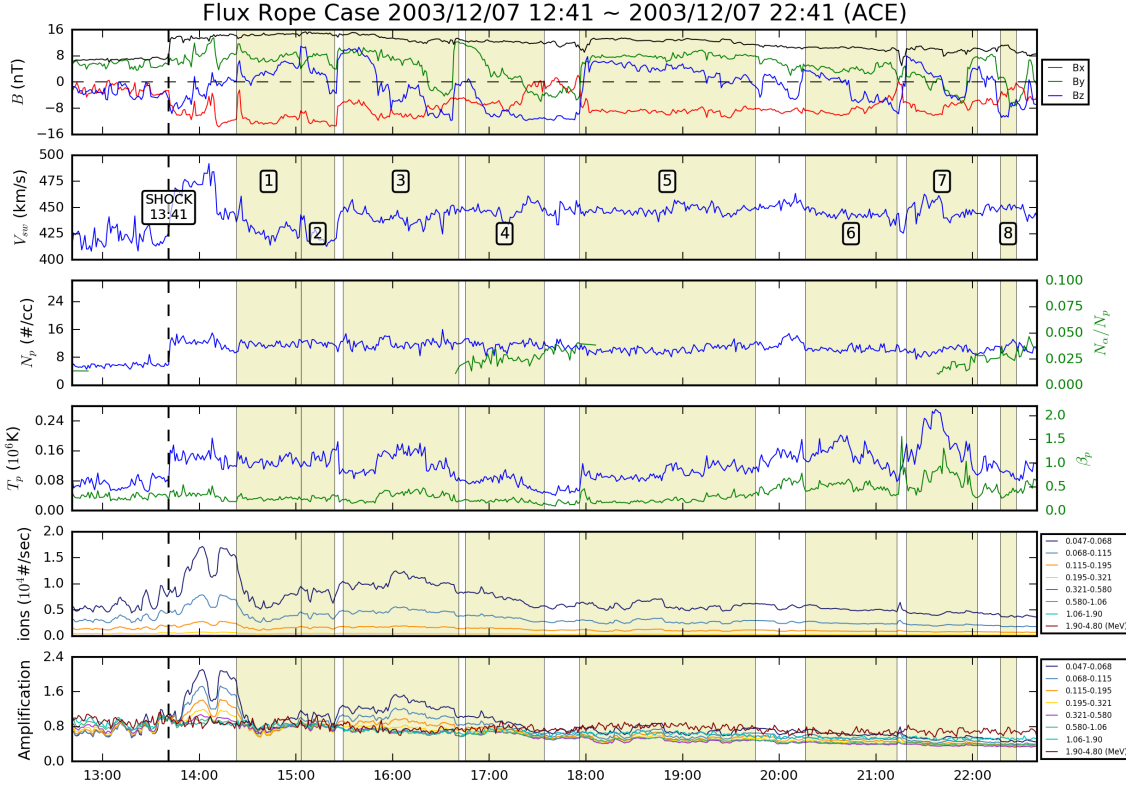


**Figure 5.10:** Time series data (ACE) from Dec. 7, 2003, 12:41 UT to Dec. 7, 2003, 22:41 UT. The format is the same as Figure 5.3.

during a time period when the spacecraft ACE and Wind were radially aligned. Figure 5.10 shows ACE time series data from December 7th, 2003, 12:41 UT to 22:41 UT. Figure 5.11 shows Wind time series data from December 7th, 2003, 12:00 UT to 21:00 UT. Figure 5.10 shows a shock observed at 13:41 UT. However, this shock was not observed by Wind in a later time as seen in Figure 5.11. The 5th and 6th panels in Figure 5.10 show that there are two major particle flux enhancement events during the plotted time interval. The first event is right after the shock, and the other ion flux enhancement is from 15:29 UT to 16:41 UT, during which a flux rope structure is detected and labeled as No.3. The first enhancement event is probably due to

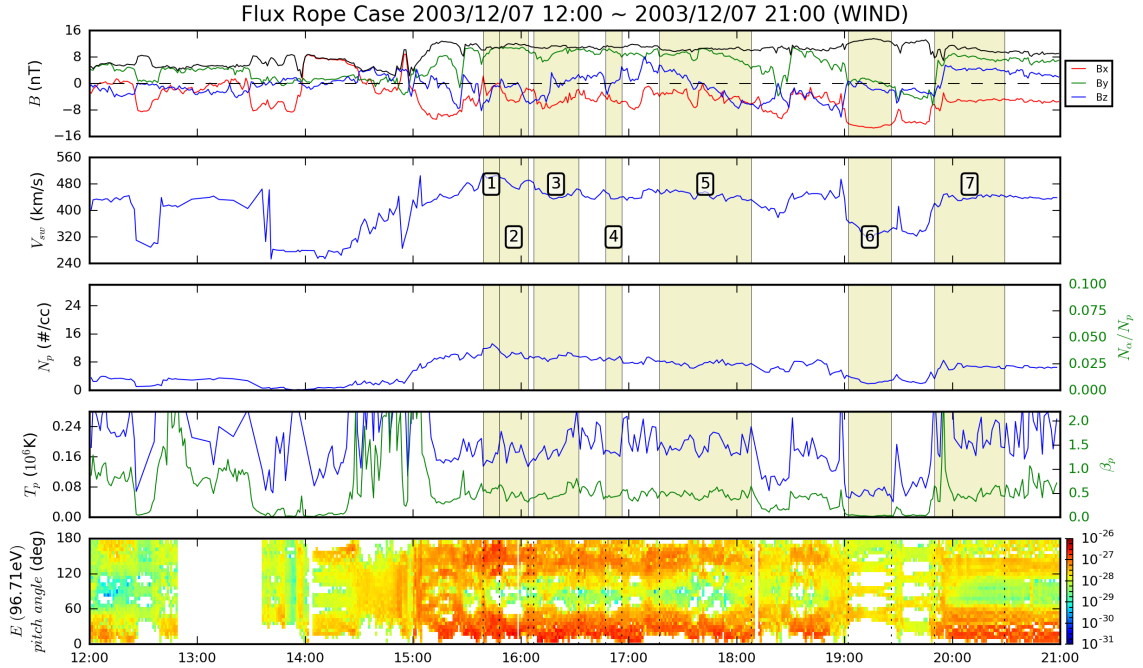


**Figure 5.11:** Time series data (Wind) from Dec. 7, 2003, 12:00 UT to Dec. 7, 2003, 21:00 UT. The format is the same as Figure 5.4.

direct shock acceleration, while the second enhancement event may be caused by flux rope related acceleration [78, 81, 105]. Next, we will check the temporal evolution of flux rope No.3 identified in Figure 5.10. If this flux rope shows a contracting feature when propagating, it could have the ability to boost the ion flux. From the Wind spacecraft data displayed in Figure 5.11, we found a possible correspondence to flux rope No.3 in Figure 5.10, whose time interval is from 17:17 UT to 18:08 UT and labeled as No.5. Using the same method as we used in the last case study, we are going to verify the correspondence by checking the ACE and Wind positions and the flux rope propagating time.

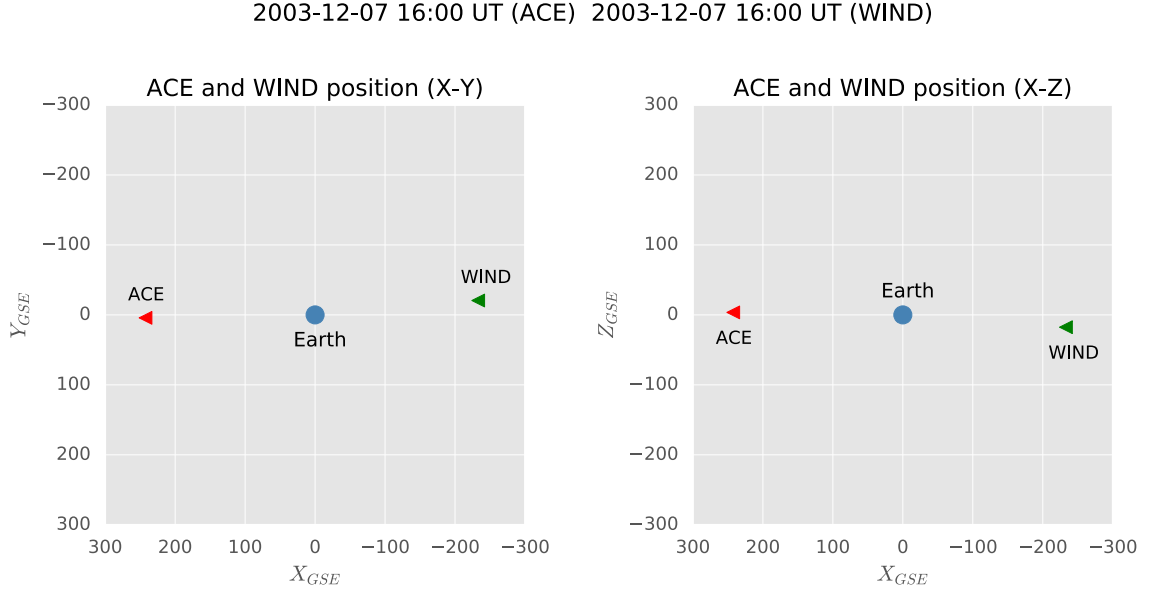
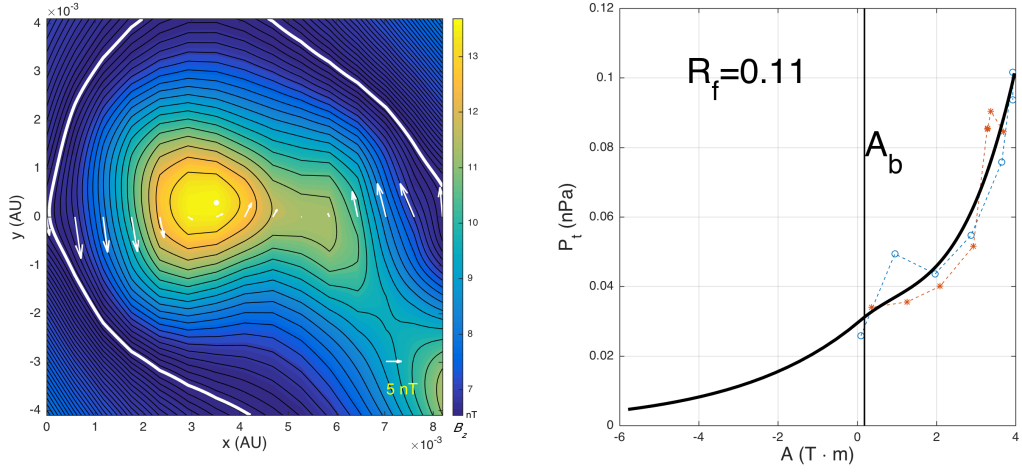


**Figure 5.12:** The positions of ACE and Wind spacecraft in the GSE coordinate system. The left panel is the projection on the XY-plane, and the right panel is the projection on the XZ-plane. Both time stamps of ACE and Wind are July 12th, 2003, 16:00 UT. The unit of all axes is Earth radius.

Figure 5.12 shows that ACE and Wind were aligned along the  $X_{GSE}$  axis and located on the noon and midnight sides of the Earth, respectively. The GSE coordinates of ACE are  $(X, Y, Z) = (1.54422 \times 10^6, 2.68164 \times 10^4, 2.28218 \times 10^4)$  km, and the GSE coordinates of Wind are  $(X, Y, Z) = (-1.4851 \times 10^6, -1.3105 \times 10^5, -1.1180 \times 10^5)$  km. The separation of ACE and Wind in the  $X_{GSE}$  direction is  $3.02932 \times 10^6$  km. The second panels of Figure 5.10 and Figure 5.11 show that the average solar wind speed during the interval of flux rope No.3 in Figure 5.10 and flux rope No.5 in Figure 5.11 is about 440 km/s. So the propagating time for the flux rope from ACE to Wind is about 115 minutes. The center time of flux rope No.3 in Figure 5.10 is 16:05 UT, and the center time of flux rope No.5 in Figure 5.11 is 17:43



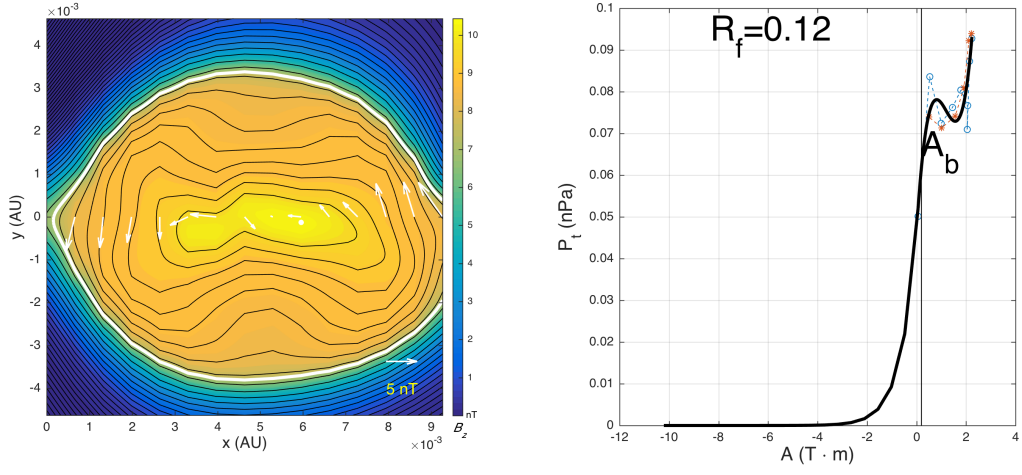
(a)  $\hat{\mathbf{z}} = [-0.8586, 0.4957, -0.1305]$

(b)

**Figure 5.13:** GS reconstruction result for flux rope record No.3 (2003 Dec. 7, 15:29  $\sim$  16:41 UT) in Figure 5.10. The format is the same as Figure 5.6.

UT. The center time shift is 98 minutes, which is close to the estimated propagating time, 115 minutes, given the relatively large separation distance in this case. Now we confirm that the flux rope No.3 from ACE measurements corresponds to the flux rope No.5 from the Wind measurements.

Figure 5.13 (a) is the reconstructed cross section of flux rope No.3 in Figure 5.10. Its core  $B_z$  field is about 13.5 nT, which is strong for a small-scale flux rope. The field configuration indicates that this flux rope has right-handed chirality. This flux rope is distorted along the  $x$  direction. It looks like the relic of two merging flux ropes. Figure 5.14 (a) is the reconstructed cross section of flux rope No.5 in Figure 5.11. The core  $B_z$  field is about 10 nT, which is relatively weaker compared with its counterpart in Figure 5.13 (a). This flux rope also has right-handed chirality. This is a necessary condition to assure the correspondence between flux rope No.3



(a)  $\hat{\mathbf{z}} = [-0.2566, 0.9577, -0.1305]$

(b)

**Figure 5.14:** GS reconstruction result for flux rope record No.5 (2003 Dec. 7, 17:18 - 18:08 UT) in Figure 5.11. The format is the same as Figure 5.6.

from ACE and flux rope No.5 from Wind. Figure 5.14 (a) shows a flux rope pinched in the center. This feature can be considered to be evolved from the distorted feature in Figure 5.13 (a). By checking the axial orientations of flux rope No.3 and flux rope No.5, we find that the angle between them is  $45^\circ$ , indicating that the axial orientation changes during evolution. The scale sizes of these two flux ropes are similar, which are about  $8 \times 10^{-3}$  AU, i.e., 188 Earth radii. The overall  $B_z$  field of flux rope No.5 is lower than that of No.3, which is a reasonable phenomenon in plasma relaxation process. From Figure 5.13 (a) to Figure 5.14 (a), we can see a flux rope undergoing the end phase of a merging process, in which its chirality and scale size were kept, but the axial orientation changed by  $45^\circ$  and the overall magnetic field decreased.

The 5th panel in Figure 5.11 shows that the strong counterstreaming suprathermal electron flux appeared during the interval of flux rope No.5. The counterstream-

ing suprathermal electrons did not show up in the last case study (see the 5th panel of Figure 5.4, in the interval of flux rope No.7). Also we note that the average proton  $\beta$  of flux rope No.3 in Figure 5.10 and flux rope No.5 in Figure 5.11 is about 0.5, whereas, in the last case study, this value is higher than 1.0. The strong counter-streaming suprathermal electron flux and low proton  $\beta$  suggest that flux rope No.3 at ACE may originate from the Sun, instead of being formed in the solar wind. The ion flux within the flux rope interval in this case is also much stronger than that in the last case (see the 5th panel of Figure 5.3 and the 5th panel of Figure 5.10).

### 5.3 Summary and Discussion

In this chapter, we presented the preliminary statistical results based on the association of interplanetary shocks with our newly-built small-scale flux rope database. The comparison studies showed that the flux ropes downstream shocks do not show obvious evidence indicating that they are created locally by shocks. Instead, they are just a likely subset of the ordinary flux rope population.

With the combined observations of ACE and Wind spacecraft, we analyzed the radial evolution of flux ropes and the effect on particle energization. Two case studies were presented, in which the flux rope merging process and the particle energization were observed. In the first case study, we see that a twin flux rope structure was observed by ACE which then became one single flux rope when it was observed by Wind 58 minutes later. In the second case study, we showed the end phase of a flux rope merging process. In both cases, the energetic ions flux was enhanced during the

flux rope merging process. These two cases suggest that the flux rope dynamics may play an important role in local particle energization.

## CHAPTER 6

### CONCLUSIONS

#### 6.1 Summary of Work in This Dissertation

In Chapter 1, we briefly reviewed the structures and transients in the heliosphere, including the solar wind properly characterized by its speed variation over all latitudes in different phases of the solar cycle, and an overview of CMEs, ICMEs, HCSs, CIRs, MCs, and small-scale magnetic flux ropes. We reviewed the research on MCs and small-scale magnetic flux ropes, and discussed the difference in properties, origins, and creation mechanisms between MCs and small-scale magnetic flux ropes. We summarized the two different views on the origin and the creation mechanism of small-scale flux ropes. We did a thorough literature review on the small-scale magnetic flux ropes, and summarized the current research advance, as well as the major problems. Small-scale magnetic flux ropes are believed to have the ability to accelerate particles in appropriate energy bands. We summarized the research on particle acceleration by small-scale flux ropes, and discussed the relevant theories and models. We presented our research objectives and the methodology. At the end of this chapter, we showed the organization of this dissertation.

In Chapter 2, we introduced the Grad-Shafranov (GS) reconstruction technique. We elaborated in detail on the theoretical basis of the GS reconstruction. Then we applied the GS reconstruction method to small-scale magnetic flux ropes and presented three GS reconstruction examples.

In Chapter 3, we developed a new automated small-scale magnetic flux rope detection algorithm based on the GS reconstruction technique. We described in great detail the development process of the automated flux rope detection algorithm, in terms of (1) the choice of appropriate frame of reference, (2) the determination of flux rope axial orientation, (3) the multiple iteration strategy, (4) the ground rules in the detection process, and (5) the core procedure in the flux rope detection algorithm. A detailed flow chart was developed to illustrate the procedures of the detection process. The core procedure was especially laid out and explained in adequate detail. After the initial detection process, a cleanup procedure was performed to remove overlaps and combine the flux rope records obtained from different iterations with different data window widths. The greedy algorithm was adopted to combine the flux rope records. The last step was to apply some additional criteria to remove non-flux rope structures. The Walén test was applied in order to remove Alfvénic structures, and the average magnetic field magnitude greater than or equal to 5 nT was set as a criterion to exclude small fluctuations. In the last section of Chapter 3, we presented our end product, the online database of small-scale magnetic flux ropes. The structure and contents of the website hosting the database were described.

In Chapter 4, we performed the statistical analysis of small-scale magnetic flux rope events based on our newly developed database. We investigated the statistical

properties of small-scale magnetic flux ropes in terms of (1) the occurrence rate over time, (2) the axial orientations, (3) the solar wind speed distribution, (4) the duration and scale size distributions, (5) the proton temperature and density, (6) the plasma beta, (7) the waiting time distribution, (8) the wall to wall time distribution, and (9) the distance to HCSs. We discussed the different properties of flux ropes under different solar wind speed conditions. In particular, we presented the WTD analysis and discussed the possible origination and generation mechanisms of small-scale magnetic flux ropes in comparison with other relevant studies.

In Chapter 5, we first performed the basic statistical analysis of the flux ropes detected downstream of interplanetary shocks, and found that these flux ropes exhibit similar statistical properties to the bulk of events presented in Chapter 4. Then, with the combined observations of the ACE and Wind spacecraft, we analyzed the temporal evolution of flux ropes and the effect to particle energization. Two case studies were presented, in which the flux rope merging process and the particle energization were observed. In the first case study, a twin flux rope structure was observed by ACE which then became one single flux rope when it was observed by Wind 58 minutes later. In the second case study, we showed the end phase of a flux rope merging process. In both cases, the energetic ions flux was enhanced during the flux rope merging process. These two cases suggested that the flux rope dynamics may play an important role in local particle energization.

Chapter 6 is the current chapter. In this chapter we summarize the work we have done, the results we obtained, and the future work plan.

## 6.2 New Results in This Dissertation

In this dissertation, we have developed a new approach for small-scale magnetic flux rope detection, and applied this approach to Wind spacecraft data to detect small-scale magnetic flux ropes in the solar wind at 1 AU. We successfully detected 74,241 small-scale flux rope events from 1996 to 2016, covering two solar cycles. This large number of small-scale flux ropes has not been discovered by any other detection approach or in any other previous studies. We build and maintain a flux rope database online to provide science community free access to this database via <http://fluxrope.info>. By developing this database, we have contributed to the new knowledge for the physics of the heliosphere, gained through the investigation of the particular type of space plasma structures, the magnetic flux ropes. We foresee that this database will benefit future studies on space plasma processes in the heliosphere.

Using this database, we performed the statistical analysis as well as individual case studies on small-scale magnetic flux ropes, and obtained a number of significant results listed below:

1. The occurrence of small-scale flux ropes has strong solar cycle dependency.

This is consistent with the occurrence of magnetic clouds, which indicates the possibility that the small-scale flux ropes, at least a portion of them, may share the same generation mechanism as magnetic clouds.

2. The small-scale flux ropes tend to align along the Parker spiral, in the ecliptic plane. This is consistent with the orientation pattern of “flux tubes”. This indicates that they belong to the general population of “flux tubes”.

3. The small-scale flux ropes show different statistical properties under different solar wind speed conditions. In low speed ( $< 400$  km/s) solar wind, the flux ropes tend to have lower proton temperature, and higher proton number density, and there are relatively more events near the HCSs. In high speed ( $\geq 400$  km/s) solar wind, they tend to have higher proton temperature and lower proton number density. The events tend to occur in the vicinity of HCSs,  $\sim 1$  day later.
4. The flux rope duration and scale size have an approximately linear relation. Both the duration and scale size distributions obey the power law. The power index close to  $-2$  suggests that the larger scale size flux ropes ( $0.01 \sim 0.05$  AU) in our database under the condition of relatively high speed solar wind ( $\bar{V}_{sw} \geq 400$  km/s) may have closer relation to a solar source than the small-scale flux ropes under other conditions.
5. From the waiting time analysis, we found that the distribution for the shorter waiting time can be fitted by an exponential function, indicating that these flux ropes may undergo the pure Poisson process. The distribution associated with longer waiting time can be fitted by a power law function, indicating the clustering behavior of these flux ropes. The different behaviors between the flux ropes with shorter waiting time and the ones with longer waiting time reveal the clue implying that they may belong to two different populations, but may still share the same origination mechanism. The breakpoint is at  $60 \sim 80$  minutes.

6. The wall-to-wall time distribution obeys double power law with the break point at 60 minutes around the scale size of typical correlation length in solar wind turbulence. This result is the same as the WTDs from MHD turbulence simulations for the inertia range that is covered by the scale size range in our database. Through our unique approach, we provide the direct evidence in supporting the view of locally generated coherent structures intrinsic to the dynamic processes in the solar wind as manifested by magnetic reconnection and inverse turbulence cascade.
7. The study of the locations of small-scale flux ropes with respect to the HCSs shows that the small-scale magnetic flux ropes tend to accumulate near the HCSs, especially for the flux ropes under slow solar wind condition. This has been considered as an evidence supporting the view that the small-scale flux ropes are created locally across the heliospheric current sheets. Alternatively, this also seems to support the contradicting view that these small-scale flux ropes originate from streamer belts near the Sun where the HCS originates. Therefore the HCS serves as a conduit for them to propagate and reach 1 AU, while exhibiting signatures of low speed, high density and low temperature, as observed in-situ.
8. Some additional statistics show that the small-scale flux ropes with larger scale size tend to have low proton temperature, and tend to appear in slow speed solar wind. These behaviors, especially the former, are similar to MCs.

9. Preliminary analysis with full GS reconstruction of magnetic flux rope configurations shows the evidence that the adjacent small-scale flux ropes are subject to merging. Additionally, the merging flux ropes are able to energize particles.
10. Flux ropes do exist downstream of interplanetary shocks. The analysis on the ions flux enhancement within the flux rope intervals downstream of shocks shows the evidence that the merging edges of adjacent flux ropes coincide with the peak of enhanced ions flux.

### 6.3 Future Work

To further develop and expand our small-scale flux rope database, additional work can be done as listed below:

1. The duration range of the flux ropes in our database is from 9 minutes to 361 minutes. It is desirable to extend our analysis to longer durations, bridging the gap between the upper limit of our current analysis ( $\sim$ 6 hours), to the lower end of the MCs durations ( $\sim$ 12 hours). Due to the expandable flexibility in the architectural design of the detection algorithm, extending the database can be readily achieved by running additional iterations with longer detection windows. The extension to smaller durations can also be achieved by using higher-resolution in-situ measurements from the existing and future spacecraft missions.
2. Our database is based on the in-situ data from Wind spacecraft. The flux rope detection algorithm can be applied to any other data source without major

modification. We just need to preprocess the magnetic field data and feed them into the detection program. For example, the data from ACE spacecraft can be used to detect more flux ropes at 1 AU. We can compare the events observed by Wind spacecraft with those observed by ACE spacecraft. When the two spacecraft locations are separated by appropriate distances, we can use them to study the small-scale flux rope evolution process just as what we did in Chapter 5.

3. We can extend the flux rope searching region from near ecliptic at 1 AU to inner or outer heliosphere of different heliocentric distances by using other spacecraft missions, such as Ulysses. In addition, the Ulysses spacecraft can provide data for us to detect small-scale flux ropes in higher latitudes other than the ecliptic plane. This is particularly promising for future applications to the highly anticipated Parker Solar Probe and Solar Orbiter missions.

To further utilize our small-scale flux rope database to study relevant space physics problems, there are following possible applications:

1. Statistical analysis can be further performed to investigate the relation between small-scale flux ropes and energetic particles, CMEs, flares, MHD turbulence, and other transient structures.
2. The question regarding origination of the small-scale flux ropes is partially answered in this dissertation. We speculate that some small-sale flux ropes may have closer relation to a solar source, and some are more likely to be created

locally. Further work needs to be done to clearly distinguish these two scenarios and to find their source correspondence and more specific conditions under which they occur in order to verify their association with the specific generation mechanism.

3. The detailed case studies, including observational analysis and reconstruction of flux ropes, theoretical analysis and numerical simulation, can be performed to investigate the flux rope dynamic process and its effect on other space plasma processes.
4. The magnetospheric substorm is more likely to be affected by small-scale magnetic flux ropes, since it accumulates energy gradually and releases energy suddenly. There is some preliminary evidence suggesting the relation between small-scale magnetic flux ropes and substorms. A comprehensive statistical study can be performed by using the large number of events in our database and the substorm event lists from other sources. Also, the substorm activity is closely related to the enhancement of the relativistic electron flux in the radiation belt. The better prediction models for substorms and relativistic electron flux can be expected if the correlations with small-scale flux ropes are established.

## REFERENCES

- [1] E. N. Parker. Dynamics of the Interplanetary Gas and Magnetic Fields. *The Astrophysical Journal*, 128:664, November 1958.
- [2] D. J. McComas, H. A. Elliott, N. A. Schwadron, J. T. Gosling, R. M. Skoug, and B. E. Goldstein. The three-dimensional solar wind around solar maximum. *Geophysical Research Letters*, 30(10), 2003. 1517.
- [3] J. M. Wilcox and P. H. Scherrer. Annual and solar-magnetic-cycle variations in the interplanetary magnetic field, 1926-1971. *Journal of Geophysical Research: Space Physics*, 77:5385, 1972.
- [4] L. Davis, Jr. The Interplanetary Magnetic Field. *NASA Special Publication*, 308:93, 1972.
- [5] Michael Schulz. Interplanetary sector structure and the heliomagnetic equator. *Astrophysics and Space Science*, 24(2):371–383, Oct 1973.
- [6] L. Svalgaard. On the use of Godhavn H component as an indicator of the interplanetary sector polarity. *Journal of Geophysical Research: Space Physics*, 80:2717–2722, July 1975.
- [7] E. J. Smith, B. T. Tsurutani, and R. L. Rosenberg. Observations of the interplanetary sector structure up to heliographic latitudes of 16 deg - Pioneer 11. *Journal of Geophysical Research: Space Physics*, 83:717–724, February 1978.
- [8] E. J. Smith. The heliospheric current sheet. *Journal of Geophysical Research: Space Physics*, 106:15819–15832, August 2001.
- [9] Vikram Sarabhai. Some consequences of nonuniformity of solar wind velocity. *Journal of Geophysical Research*, 68(5):1555–1557, 1963.
- [10] G. L. Siscoe. Structure and orientations of solar-wind interaction fronts: Pioneer 6. *Journal of Geophysical Research*, 77(1):27–34, 1972.
- [11] J. T. Gosling, A. J. Hundhausen, V. Pizzo, and J. R. Asbridge. Compressions and rarefactions in the solar wind: Vela 3. *Journal of Geophysical Research*, 77(28):5442–5454, 1972.
- [12] A. J. Hundhausen. Coronal Expansion and Solar Wind. *Physics and Chemistry in Space*, 5, 1972.

- [13] E. J. Smith and J. H. Wolfe. Observations of interaction regions and corotating shocks between one and five AU: Pioneers 10 and 11. *Geophysical Research Letters*, 2:137–140, 1976.
- [14] V. Pizzo. A three-dimensional model of corotating streams in the solar wind, 1. theoretical foundations. *Journal of Geophysical Research: Space Physics*, 83(A12):5563–5572, 1978.
- [15] Victor J. Pizzo. A three-dimensional model of corotating streams in the solar wind 2. hydrodynamic streams. *Journal of Geophysical Research: Space Physics*, 85(A2):727–743, 1980.
- [16] Victor J. Pizzo. A three-dimensional model of corotating streams in the solar wind: 3. magnetohydrodynamic streams. *Journal of Geophysical Research: Space Physics*, 87(A6):4374–4394, 1982.
- [17] J. T. Gosling. Corotating and transient solar wind flows in three dimensions. *Annual Review of Astronomy and Astrophysics*, 34(1):35–73, 1996.
- [18] J.T. Gosling and V.J. Pizzo. Formation and evolution of corotating interaction regions and their three dimensional structure. *Space Science Reviews*, 89(1):21–52, Jul 1999.
- [19] Timothy A. Howard and S. James Tappin. Interplanetary coronal mass ejections observed in the heliosphere: 1. review of theory. *Space Science Reviews*, 147(1):31–54, Oct 2009.
- [20] S. James Tappin and Timothy A. Howard. Interplanetary coronal mass ejections observed in the heliosphere: 2. model and data comparison. *Space Science Reviews*, 147(1):55, Jun 2009.
- [21] Timothy A. Howard and S. James Tappin. Interplanetary coronal mass ejections observed in the heliosphere: 3. physical implications. *Space Science Reviews*, 147(1):89, Oct 2009.
- [22] R. G. Stone and B. T. Tsurutani. Collisionless shocks in the heliosphere: A tutorial review. *Washington DC American Geophysical Union Geophysical Monograph Series*, 34, 1985.
- [23] Robert G. Tsurutani, Bruce T.; Stone. Collisionless shocks in the heliosphere: Reviews of current research. *Eos, Transactions American Geophysical Union*, 66(48):1200–1200, 1985.
- [24] Andr Balogh and Rudolf A Treumann. *Physics of Collisionless Shocks: Space Plasma Shock Waves*. ISSI Scientific Report Series. Springer, New York, 2013.
- [25] Thomas H. Zurbuchen and Ian G. Richardson. In-situ solar wind and magnetic field signatures of interplanetary coronal mass ejections. *Space Science Reviews*, 123(1):31–43, Mar 2006.

- [26] Qiang Hu. The grad-shafranov reconstruction in twenty years: 1996–2016. *Science China Earth Sciences*, 60(8):1466–1494, Aug 2017.
- [27] T. Gold and F. Hoyle. On the origin of solar flares. *Monthly Notices of the Royal Astronomical Society*, 120:89, 1960.
- [28] L. Burlaga, E. Sittler, F. Mariani, and R. Schwenn. Magnetic loop behind an interplanetary shock: Voyager, helios, and imp 8 observations. *Journal of Geophysical Research: Space Physics*, 86(A8):6673–6684, 1981.
- [29] E. R. Priest, A. W. Hood, and U. Anzer. A twisted flux-tube model for solar prominences. I - General properties. *The Astrophysical Journal*, 344:1010–1025, September 1989.
- [30] D. M. Rust and A. Kumar. Helical magnetic fields in filaments. *Solar Physics*, 155:69–97, November 1994.
- [31] B. C. Low. Solar Activity and the Corona. *Solar Physics*, 167:217–265, August 1996.
- [32] B. W. Lites, B. C. Low, V. Martinez Pillet, P. Seagraves, A. Skumanich, Z. A. Frank, R. A. Shine, and S. Tsuneta. The Possible Ascent of a Closed Magnetic System through the Photosphere. *The Astrophysical Journal*, 446:877, June 1995.
- [33] Y. Fan. The emergence of a twisted -tube into the solar atmosphere. *The Astrophysical Journal Letters*, 554(1):L111, 2001.
- [34] S. E. Gibson, L. Fletcher, G. Del Zanna, C. D. Pike, H. E. Mason, C. H. Mandrini, P. Dmoulin, H. Gilbert, J. Burkepile, T. Holzer, D. Alexander, Y. Liu, N. Nitta, J. Qiu, B. Schmieder, and B. J. Thompson. The structure and evolution of a sigmoidal active region. *The Astrophysical Journal*, 574(2):1021, 2002.
- [35] W. Manchester IV, T. Gombosi, D. DeZeeuw, and Y. Fan. Eruption of a buoyantly emerging magnetic flux rope. *The Astrophysical Journal*, 610(1):588, 2004.
- [36] T. Magara. Dynamic and topological features of photospheric and coronal activities produced by flux emergence in the sun. *The Astrophysical Journal*, 653(2):1499, 2006.
- [37] Takenori J. Okamoto, Saku Tsuneta, Bruce W. Lites, Masahito Kubo, Takaaki Yokoyama, Thomas E. Berger, Kiyoshi Ichimoto, Yukio Katsukawa, Shinichi Nagata, Kazunari Shibata, Toshifumi Shimizu, Richard A. Shine, Yoshinori Suematsu, Theodore D. Tarbell, and Alan M. Title. Emergence of a helical flux rope under an active region prominence. *The Astrophysical Journal Letters*, 673(2):L215, 2008.

- [38] Y. Fan. On the eruption of coronal flux ropes. *The Astrophysical Journal*, 719(1):728, 2010.
- [39] P. N. Brandt, G. B. Scharmer, S. Ferguson, R. A. Shine, and T. D. Tarbell. Vortex flow in the solar photosphere. *Nature*, 335:238–240, September 1988.
- [40] A. A. van Ballegooijen and P. C. H. Martens. Formation and eruption of solar prominences. *Astrophysical Journal*, 343:971–984, August 1989.
- [41] L. M. Green and B. Kliem. Flux rope formation preceding coronal mass ejection onset. *The Astrophysical Journal Letters*, 700(2):L83, 2009.
- [42] G. Aulanier, T. Trk, P. Dmoulin, and E. E. DeLuca. Formation of torus-unstable flux ropes and electric currents in erupting sigmoids. *The Astrophysical Journal*, 708(1):314, 2010.
- [43] T. Amari, J.-J. Aly, J.-F. Luciani, Z. Mikic, and J. Linker. Coronal mass ejection initiation by converging photospheric flows: Toward a realistic model. *The Astrophysical Journal Letters*, 742(2):L27, 2011.
- [44] E. W. Hones and K. Schindler. Magnetotail plasma flow during substorms: A survey with imp 6 and imp 8 satellites. *Journal of Geophysical Research: Space Physics*, 84(A12):7155–7169, 1979.
- [45] Mark B. Moldwin and W. Jeffrey Hughes. Plasmoid observations in the distant plasma sheet boundary layer. *Geophysical Research Letters*, 19(19):1911–1914, 1992.
- [46] Mark B. Moldwin and W. Jeffrey Hughes. On the formation and evolution of plasmoids: A survey of isee 3 geotail data. *Journal of Geophysical Research: Space Physics*, 97(A12):19259–19282, 1992.
- [47] Mark B. Moldwin and W. Jeffrey Hughes. Geomagnetic substorm association of plasmoids. *Journal of Geophysical Research: Space Physics*, 98(A1):81–88, 1993.
- [48] T. Nagai, M. Fujimoto, R. Nakamura, Y. Saito, T. Mukai, T. Yamamoto, A. Nishida, S. Kokubun, G. D. Reeves, and R. P. Lepping. Geotail observations of a fast tailward flow at  $x_{\text{gsm}} = 15$  re. *Journal of Geophysical Research: Space Physics*, 103(A10):23543–23550, 1998.
- [49] J. A. Slavin, R. P. Lepping, J. Gjerloev, D. H. Fairfield, M. Hesse, C. J. Owen, M. B. Moldwin, T. Nagai, A. Ieda, and T. Mukai. Geotail observations of magnetic flux ropes in the plasma sheet. *Journal of Geophysical Research: Space Physics*, 108(A1):SMP 10–1–SMP 10–18, 2003. 1015.

- [50] J. A. Slavin, R. P. Lepping, J. Gjerloev, M. L. Goldstein, D. H. Fairfield, M. H. Acuna, A. Balogh, M. Dunlop, M. G. Kivelson, K. Khurana, A. Fazakerley, C. J. Owen, H. Reme, and J. M. Bosqued. Cluster electric current density measurements within a magnetic flux rope in the plasma sheet. *Geophysical Research Letters*, 30(7), 2003. 1362.
- [51] J. P. Eastwood, D. G. Sibeck, J. A. Slavin, M. L. Goldstein, B. Lavraud, M. Sitnov, S. Imber, A. Balogh, E. A. Lucek, and I. Dandouras. Observations of multiple x-line structure in the earth's magnetotail current sheet: A cluster case study. *Geophysical Research Letters*, 32(11), 2005. L11105.
- [52] M. B. Moldwin, J. L. Phillips, J. T. Gosling, E. E. Scime, D. J. McComas, S. J. Bame, A. Balogh, and R. J. Forsyth. Ulysses observation of a noncoronal mass ejection flux rope: Evidence of interplanetary magnetic reconnection. *Journal of Geophysical Research: Space Physics*, 100(A10):19903–19910, 1995.
- [53] M. B. Moldwin, S. Ford, R. Lepping, J. Slavin, and A. Szabo. Small-scale magnetic flux ropes in the solar wind. *Journal of Geophysical Research: Space Physics*, 27:57–60, January 2000.
- [54] R. P. Lepping, J. A. Jones, and L. F. Burlaga. Magnetic field structure of interplanetary magnetic clouds at 1 au. *Journal of Geophysical Research: Space Physics*, 95(A8):11957–11965, 1990.
- [55] V. Bothmer and D.M. Rust. *The Field Configuration of Magnetic Clouds and the Solar Cycle*, pages 139–146. American Geophysical Union, 1997.
- [56] Charles W. Smith and John L. Phillips. The role of coronal mass ejections and interplanetary shocks in interplanetary magnetic field statistics and solar magnetic flux ejection. *Journal of Geophysical Research: Space Physics*, 102(A1):249–261, 1997.
- [57] V. Bothmer and R. Schwenn. The structure and origin of magnetic clouds in the solar wind. *Annales Geophysicae*, 16(1):1–24, 1998.
- [58] A. Wilson, editor. *Proc. Sources of magnetic helicity over the solar cycle*, 2003.
- [59] Robert J. Leamon, Richard C. Canfield, Sarah L. Jones, Keith Lambkin, Brian J. Lundberg, and Alexei A. Pevtsov. Helicity of magnetic clouds and their associated active regions. *Journal of Geophysical Research: Space Physics*, 109(A5), 2004. A05106.
- [60] D. E. Innes, A. Lagg, and S. K. Solanki, editors. *Proc. Quantitative Link Between Solar Ejecta and Interplanetary Magnetic Clouds: Magnetic Helicity*, 2003.
- [61] V. J. Pizzo, T. E. Holzer, and D. G. Sime, editors. *Proc. The origin and propagation of coronal mass ejections*, 2003.

- [62] I. G. Richardson and H. V. Cane. The fraction of interplanetary coronal mass ejections that are magnetic clouds: Evidence for a solar cycle variation. *Geophysical Research Letters*, 31(18), 2004. L18804.
- [63] T. Mulligan, C. T. Russell, and J. G. Luhmann. Solar cycle evolution of the structure of magnetic clouds in the inner heliosphere. *Geophysical Research Letters*, 25(15):2959–2962, 1998.
- [64] B. J. Lynch, J. R. Gruesbeck, T. H. Zurbuchen, and S. K. Antiochos. Solar cycledependent helicity transport by magnetic clouds. *Journal of Geophysical Research: Space Physics*, 110(A8), 2005. A08107.
- [65] L. F. Burlaga and K. W. Behannon. Magnetic clouds: Voyager observations between 2 and 4 au. *Solar Physics*, 81(1):181–192, 1982.
- [66] L. W. Klein and L. F. Burlaga. Interplanetary magnetic clouds at 1 au. *Journal of Geophysical Research: Space Physics*, 87(A2):613–624, 1982.
- [67] R. P. Lepping, D. B. Berdichevsky, C.-C. Wu, A. Szabo, T. Narock, F. Mariani, A. J. Lazarus, and A. J. Quivers. A summary of wind magnetic clouds for years 1995-2003: model-fitted parameters, associated errors and classifications. *Annales Geophysicae*, 24:215–245, March 2006.
- [68] Yuming Wang, Zhenjun Zhou, Chenglong Shen, Rui Liu, and S. Wang. Investigating plasma motion of magnetic clouds at 1 au through a velocity-modified cylindrical force-free flux rope model. *Journal of Geophysical Research: Space Physics*, 120(3):1543–1565, 2015. 2014JA020494.
- [69] H. Q. Feng, D. J. Wu, and J. K. Chao. Size and energy distributions of interplanetary magnetic flux ropes. *Journal of Geophysical Research: Space Physics*, 112(A2), 2007. A02102.
- [70] M. L. Cartwright and M. B. Moldwin. Comparison of small-scale flux rope magnetic properties to large-scale magnetic clouds: Evidence for reconnection across the hcs? *Journal of Geophysical Research: Space Physics*, 113(A9), 2008. A09105.
- [71] H. Q. Feng, D. J. Wu, C. C. Lin, J. K. Chao, L. C. Lee, and L. H. Lyu. Interplanetary small- and intermediate-sized magnetic flux ropes during 19952005. *Journal of Geophysical Research: Space Physics*, 113(A12):A12105, December 2008. A12105.
- [72] M. L. Cartwright and M. B. Moldwin. Heliospheric evolution of solar wind small-scale magnetic flux ropes. *Journal of Geophysical Research (Space Physics)*, 115(A8):A08102, August 2010. A08102.
- [73] H. Q. Feng, G. Q. Zhao, and J. M. Wang. Counterstreaming electrons in small interplanetary magnetic flux ropes. *Journal of Geophysical Research: Space Physics*, 120(12):10,175–10,184, 2015. 2015JA021643.

- [74] J. F. Drake, M. Swisdak, H. Che, and M. A. Shay. Electron acceleration from contracting magnetic islands during reconnection. *Nature*, 443:553–556, October 2006.
- [75] J. F. Drake, M. Swisdak, K. M. Schoeffler, B. N. Rogers, and S. Kobayashi. Formation of secondary islands during magnetic reconnection. *Geophysical Research Letters*, 33(13), 2006. L13105.
- [76] J. Drake, M. Opher, M. Swisdak, and J. Chamoun. A magnetic reconnection mechanism for the generation of anomalous cosmic rays. In *38th COSPAR Scientific Assembly*, volume 38 of *COSPAR Meeting*, page 5, 2010.
- [77] M. Oka, T.-D. Phan, S. Krucker, M. Fujimoto, and I. Shinohara. Electron Acceleration by Multi-Island Coalescence. *The Astrophysical Journal*, 714:915–926, May 2010.
- [78] G. P. Zank, J. A. le Roux, G. M. Webb, A. Dosch, and O. Khabarova. Particle acceleration via reconnection processes in the supersonic solar wind. *The Astrophysical Journal*, 797(1):28, 2014.
- [79] J A le Roux, G M Webb, G P Zank, and O Khabarova. Energetic ion acceleration by small-scale solar wind flux ropes. *Journal of Physics: Conference Series*, 642(1):012015, 2015.
- [80] G P Zank, P Hunana, P Mostafavi, J A le Roux, Gang Li, G M Webb, and O Khabarova. Particle acceleration by combined diffusive shock acceleration and downstream multiple magnetic island acceleration. *Journal of Physics: Conference Series*, 642(1):012031, 2015.
- [81] G. P. Zank, P. Hunana, P. Mostafavi, J. A. Le Roux, G. Li, G. M. Webb, O. Khabarova, A. Cummings, E. Stone, and R. Decker. Diffusive Shock Acceleration and Reconnection Acceleration Processes. *The Astrophysical Journal*, 814:137, December 2015.
- [82] O. Khabarova, G. P. Zank, G. Li, J. A. le Roux, G. M. Webb, A. Dosch, and O. E. Malandraki. Small-scale Magnetic Islands in the Solar Wind and Their Role in Particle Acceleration. I. Dynamics of Magnetic Islands Near the Heliospheric Current Sheet. *The Astrophysical Journal*, 808:181, August 2015.
- [83] Olga V. Khabarova, Gary P. Zank, Gang Li, Olga E. Malandraki, Jakobus A. le Roux, and Gary M. Webb. Small-scale magnetic islands in the solar wind and their role in particle acceleration. ii. particle energization inside magnetically confined cavities. *The Astrophysical Journal*, 827(2):122, 2016.
- [84] Olga V. Khabarova and Gary P. Zank. Energetic particles of kev-mev energies observed near reconnecting current sheets at 1 au. *The Astrophysical Journal*, 843(1):4, 2017.

- [85] H. Q. Feng, J. K. Chao, L. H. Lyu, and L. C. Lee. The relationship between small interplanetary magnetic flux rope and the substorm expansion phase. *Journal of Geophysical Research: Space Physics*, 115(A9), 2010. A09108.
- [86] X.-Y. Zhang, M.B. Moldwin, and M. Cartwright. The geo-effectiveness of interplanetary small-scale magnetic fluxropes. *Journal of Atmospheric and Solar-Terrestrial Physics*, 95:1 – 14, 2013.
- [87] A. Retinò, D. Sundkvist, A. Vaivads, F. Mozer, M. André, and C. J. Owen. In situ evidence of magnetic reconnection in turbulent plasma. *Nature Physics*, 3:236–238, April 2007.
- [88] L.-J. Chen, A. Bhattacharjee, P. A. Puhl-Quinn, H. Yang, N. Bessho, S. Imada, S. Mühlbachler, P. W. Daly, B. Lefebvre, Y. Khotyaintsev, A. Vaivads, A. Fazakerley, and E. Georgescu. Observation of energetic electrons within magnetic islands. *Nature Physics*, 4:19–23, January 2008.
- [89] L. Trenchi, R. Bruno, D. Telloni, R. D'amicis, M. F. Marcucci, T. H. Zurbuchen, and M. Weberg. Solar Energetic Particle Modulations Associated with Coherent Magnetic Structures. *The Astrophysical Journal*, 770:11, June 2013.
- [90] J. A. Tesselin, W. H. Matthaeus, M. Wan, K. T. Osman, D. Ruffolo, and J. Giacalone. Association of Suprathermal Particles with Coherent Structures and Shocks. *The Astrophysical Journal*, 776:L8, October 2013.
- [91] H. Karimabadi, V. Roytershteyn, H. X. Vu, Y. A. Omelchenko, J. Scudder, W. Daughton, A. Dimmock, K. Nykyri, M. Wan, D. Sibeck, M. Tatineni, A. Majumdar, B. Loring, and B. Geveci. The link between shocks, turbulence, and magnetic reconnection in collisionless plasmas. *Physics of Plasmas*, 21(6):062308, June 2014.
- [92] Y. Matsumoto, T. Amano, T. N. Kato, and M. Hoshino. Stochastic electron acceleration during spontaneous turbulent reconnection in a strong shock wave. *Science*, 347:974–978, February 2015.
- [93] J. A. le Roux, G. P. Zank, G. M. Webb, and O. V. Khabarova. Combining diffusive shock acceleration with acceleration by contracting and reconnecting small-scale flux ropes at heliospheric shocks. *The Astrophysical Journal*, 827(1):47, 2016.
- [94] Jinlei Zheng and Qiang Hu. Observations and analysis of small-scale magnetic flux ropes in the solar wind. *Journal of Physics: Conference Series*, 767(1):012028, 2016.
- [95] O V Khabarova, G P Zank, G Li, J A le Roux, G M Webb, O E Malandraki, and V V Zharkova. Dynamical small-scale magnetic islands as a source of local acceleration of particles in the solar wind. *Journal of Physics: Conference Series*, 642(1):012033, 2015.

- [96] O. V. Khabarova, G. P. Zank, O. E. Malandraki, G. Li, J. A. le Roux, and G. M. Webb. Observational evidence for local particle acceleration associated with magnetically confined magnetic islands in the heliosphere - a review. *Sun and Geosphere*, 12:23–30, January 2017.
- [97] A. Greco, W. H. Matthaeus, S. Servidio, P. Chuychai, and P. Dmitruk. Statistical analysis of discontinuities in solar wind ace data and comparison with intermittent mhd turbulence. *The Astrophysical Journal Letters*, 691(2):L111, 2009.
- [98] H. Karimabadi, V. Roytershteyn, M. Wan, W. H. Matthaeus, W. Daughton, P. Wu, M. Shay, B. Loring, J. Borovsky, E. Leonardis, S. C. Chapman, and T. K. M. Nakamura. Coherent structures, intermittent turbulence, and dissipation in high-temperature plasmas. *Physics of Plasmas*, 20(1):012303, January 2013.
- [99] K. T. Osman, W. H. Matthaeus, J. T. Gosling, A. Greco, S. Servidio, B. Hnat, S. C. Chapman, and T. D. Phan. Magnetic Reconnection and Intermittent Turbulence in the Solar Wind. *Physical Review Letters*, 112(21):215002, May 2014.
- [100] J. A. Tassein, D. Ruffolo, W. H. Matthaeus, M. Wan, J. Giacalone, and M. Neugebauer. Effect of Coherent Structures on Energetic Particle Intensity in the Solar Wind at 1 AU. *The Astrophysical Journal*, 812:68, October 2015.
- [101] M. Neugebauer and J. Giacalone. Energetic particles, tangential discontinuities, and solar flux tubes. *Journal of Geophysical Research (Space Physics)*, 120:8281–8287, October 2015.
- [102] J. A. Tassein, D. Ruffolo, W. H. Matthaeus, and M. Wan. Local modulation and trapping of energetic particles by coherent magnetic structures. *Geophysical Research Letters*, 43:3620–3627, April 2016.
- [103] G. P. Zank, L. Adhikari, P. Hunana, D. Shiota, R. Bruno, and D. Telloni. Theory and transport of nearly incompressible magnetohydrodynamic turbulence. *The Astrophysical Journal*, 835(2):147, 2017.
- [104] J. E. Borovsky. Flux tube texture of the solar wind: Strands of the magnetic carpet at 1 AU? *Journal of Geophysical Research (Space Physics)*, 113:A08110, August 2008.
- [105] J. A. le Roux, G. P. Zank, G. M. Webb, and O. Khabarova. A kinetic transport theory for particle acceleration and transport in regions of multiple contracting and reconnecting inertial-scale flux ropes. *The Astrophysical Journal*, 801(2):112, 2015.

- [106] R. Bruno, V. Carbone, P. Veltri, E. Pietropaolo, and B. Bavassano. Identifying intermittency events in the solar wind. *Planetary Space Science*, 49:1201–1210, October 2001.
- [107] B. Neugebauer, editor. *Proc. On the field configuration in magnetic clouds*. NASA Conf. Publ., NASA CP-2280, 1983.
- [108] L. F. Burlaga. Magnetic clouds and force-free fields with constant alpha. *Journal of Geophysical Research: Space Physics*, 93(A7):7217–7224, 1988.
- [109] S. Lundquist. Magnetohydrostatic fields. *Ark. Fys.*, 2:361–365, 1950.
- [110] Q. Hu and B. U. Ö. Sonnerup. Reconstruction of magnetic flux ropes in the solar wind. *Geophysical Research Letters*, 28:467–470, 2001.
- [111] Qiang Hu and Bengt U. Ö. Sonnerup. Reconstruction of magnetic clouds in the solar wind: Orientations and configurations. *Journal of Geophysical Research: Space Physics*, 107(A7):SSH 10–1–SSH 10–15, 2002.
- [112] B. U. Ö. Sonnerup and M. Guo. Magnetopause transects. *Geophysical Research Letters*, 23(25):3679–3682, 1996.
- [113] L.-N. Hau and Bengt U. Ö. Sonnerup. Two-dimensional coherent structures in the magnetopause: Recovery of static equilibria from single-spacecraft data. *Journal of Geophysical Research: Space Physics*, 104(A4):6899–6917, 1999.
- [114] Q. Hu, C. W. Smith, N. F. Ness, and R. M. Skoug. Double flux-rope magnetic cloud in the solar wind at 1 AU. *Geophysical Research Letters*, 30:1385, April 2003.
- [115] Qiang Hu, Charles W. Smith, Norman F. Ness, and Ruth M. Skoug. Multiple flux rope magnetic ejecta in the solar wind. *Journal of Geophysical Research: Space Physics*, 109(A3), 2004. A03102.
- [116] Q. Hu, C. W. Smith, N. F. Ness, and R. M. Skoug. On the magnetic topology of October/November 2003 events. *Journal of Geophysical Research (Space Physics)*, 110:9, September 2005.
- [117] Bengt U. Ö. Sonnerup, Hiroshi Hasegawa, Wai-Leong Teh, and Lin-Ni Hau. Grad-shafranov reconstruction: An overview. *Journal of Geophysical Research: Space Physics*, 111(A9), 2006. A09204.
- [118] Q. Hu, C. J. Farrugia, V. A. Osherovich, C. Möstl, A. Szabo, K. W. Ogilvie, and R. P. Lepping. Effect of Electron Pressure on the Grad-Shafranov Reconstruction of Interplanetary Coronal Mass Ejections. *Solar Physics*, 284:275–291, May 2013.
- [119] Q. Hu, J. Qiu, B. Dasgupta, A. Khare, and G. M. Webb. Structures of Interplanetary Magnetic Flux Ropes and Comparison with Their Solar Sources. *The Astrophysical Journal*, 793:53, September 2014.

- [120] Q. Hu, J. Qiu, and S. Krucker. Magnetic field-line lengths inside interplanetary magnetic flux ropes. *Journal of Geophysical Research: Space Physics*, 120:1, June 2015.
- [121] Q. Hu. On the Grad-Shafranov (GS) Reconstruction of Toroidal Magnetic Flux Ropes. In Linghua Wang, Roberto Bruno, Eberhard Möbius, Angelos Vourlidas, and Gary Zank, editors, *International Solar Wind 14 Conference*, volume 1720 of *AIP Conf. Series*, page 040005, 2016.
- [122] Q. Hu. The Grad-Shafranov Reconstruction of Toroidal Magnetic Flux Ropes: Method Development and Benchmark Studies. *Solar Physics*, 292:116, September 2017.
- [123] Bengt U. Ö. Sonnerup and Wai-Leong Teh. Reconstruction of two-dimensional coherent mhd structures in a space plasma: The theory. *Journal of Geophysical Research: Space Physics*, 113(A5), 2008. A05202.
- [124] F. De Hoffmann and E. Teller. Magneto-hydrodynamic shocks. *Phys. Rev.*, 80:692–703, Nov 1950.
- [125] B. U. Ö. Sonnerup, I. Papamastorakis, G. Paschmann, and H. Lühr. Magnetopause properties from ampte/irm observations of the convection electric field: Method development. *Journal of Geophysical Research: Space Physics*, 92(A11):12137–12159, 1987.
- [126] A. V. Khrabrov and B. U. Ö. Sonnerup. Error estimates for minimum variance analysis. *Journal of Geophysical Research: Space Physics*, 103(A4):6641–6651, 1998.
- [127] B. U. Sonnerup and L. J. Cahill. Magnetopause structure and attitude from explorer 12 observations. *Journal of Geophysical Research*, 72(1):171–183, 1967.
- [128] B. U. Ö. Sonnerup and M. Scheible. Minimum and Maximum Variance Analysis. *ISSI Scientific Reports Series*, 1:185–220, 1998.
- [129] A. Savitzky and M. J. E. Golay. Smoothing and differentiation of data by simplified least squares procedures. *Analytical Chemistry*, 36:1627–1639, 1964.
- [130] G. Paschmann and B. U. O. Sonnerup. Proper Frame Determination and Walen Test. *ISSI Scientific Reports Series*, 8:65–74, 2008.
- [131] N. Gopalswamy, S. Yashiro, H. Xie, S. Akiyama, and P. Mkel. Properties and geoeffectiveness of magnetic clouds during solar cycles 23 and 24. *Journal of Geophysical Research: Space Physics*, 120(11):9221–9245, 2015. 2015JA021446.
- [132] Joseph E. Borovsky. On the variations of the solar wind magnetic field about the parker spiral direction. *Journal of Geophysical Research: Space Physics*, 115(A9), 2010. A09101.

- [133] Per Bak, Chao Tang, and Kurt Wiesenfeld. Self-organized criticality: An explanation of the 1/f noise. *Phys. Rev. Lett.*, 59:381–384, Jul 1987.
- [134] E. T. Lu and R. J. Hamilton. Avalanches and the distribution of solar flares. *The Astrophysical Journal Letters*, 380:L89–L92, October 1991.
- [135] Edward T. Lu, Russell J. Hamilton, J. M. McTiernan, and Kenneth R. Bromund. Solar flares and avalanches in driven dissipative systems. *Astrophysical Journal*, 412(2):841–852, 8 1993.
- [136] L. Vlahos, M. Georgoulis, R. Kluiving, and P. Paschos. The statistical flare. *Astronomy and Astrophysics*, 299:897, July 1995.
- [137] M. K. Georgoulis and L. Vlahos. Variability of the occurrence frequency of solar flares and the statistical flare. *Astronomy and Astrophysics*, 336:721–734, August 1998.
- [138] A. L. MacKinnon and K. P. MacPherson. Nonlocal communication in self-organising models of solar flare occurrence. *Astronomy and Astrophysics*, 326:1228–1234, October 1997.
- [139] Chengzhang Li, Jianhua Yang, Chuan Li, Yun Tian, Ying Yang, and Qiwei Huang. Self-organized criticality of the solar eruptions during solar cycle 23. *Scientia Sinica Physica, Mechanica and Astronomica*, 46(2):29501, 2016.
- [140] M. S. Wheatland, P. A. Sturrock, and J. M. McTiernan. The waiting-time distribution of solar flare hard x-ray bursts. *The Astrophysical Journal*, 509(1):448, 1998.
- [141] B. Miao, B. Peng, and G. Li. Current sheets from ulysses observation. *Annales Geophysicae*, 29(2):237–249, 2011.
- [142] F. Y. Wang and Z. G. Dai. Self-organized criticality in X-ray flares of gamma-ray-burst afterglows. *Nature Physics*, 9:465–467, August 2013.
- [143] C. Li, S. J. Zhong, L. Wang, W. Su, and C. Fang. Waiting time distribution of solar energetic particle events modeled with a non-stationary poisson process. *The Astrophysical Journal Letters*, 792(2):L26, 2014.
- [144] O. Sotolongo-Costa, J. C. Antoranz, A. Posadas, F. Vidal, and A. Vzquez. Lvy flights and earthquakes. *Geophysical Research Letters*, 27(13):1965–1968, 2000.
- [145] A. Greco, P. Chuaychai, W. H. Matthaeus, S. Servidio, and P. Dmitruk. Intermittent mhd structures and classical discontinuities. *Geophysical Research Letters*, 35(19), 2008. L19111.
- [146] D. A. Biesecker. *On the Occurrence of Solar Flares Observed with the Burst and Transient Source Experiment*. PhD thesis, UNIVERSITY OF NEW HAMPSHIRE., 1994.

- [147] M. S. Wheatland. The origin of the solar flare waiting-time distribution. *The Astrophysical Journal Letters*, 536(2):L109, 2000.
- [148] Markus J. Aschwanden and James M. McTiernan. Reconciliation of waiting time statistics of solar flares observed in hard x-rays. *The Astrophysical Journal*, 717(2):683, 2010.
- [149] C. Guidorzi, S. Dichiara, F. Frontera, R. Margutti, A. Baldeschi, and L. Amati. A common stochastic process rules gamma-ray burst prompt emission and x-ray flares. *The Astrophysical Journal*, 801(1):57, 2015.
- [150] G. Pearce, A. K. Rowe, and J. Yeung. A statistical analysis of hard x-ray solar flares. *Astrophysics and Space Science*, 208(1):99–111, Oct 1993.
- [151] A. Greco, W. H. Matthaeus, S. Servidio, and P. Dmitruk. Waiting-time distributions of magnetic discontinuities: Clustering or poisson process? *Phys. Rev. E*, 80:046401, Oct 2009.
- [152] G. Boffetta, V. Carbone, P. Giuliani, P. Veltri, and A. Vulpiani. Power Laws in Solar Flares: Self-Organized Criticality or Turbulence? *Physical Review Letters*, 83:4662–4665, November 1999.
- [153] Fabio Lepreti, Vincenzo Carbone, and Pierluigi Veltri. Solar flare waiting time distribution: Varying-rate poisson or lvy function? *The Astrophysical Journal Letters*, 555(2):L133, 2001.
- [154] W. H. Matthaeus, S. Dasso, J. M. Weygand, L. J. Milano, C. W. Smith, and M. G. Kivelson. Spatial correlation of solar-wind turbulence from two-point measurements. *Phys. Rev. Lett.*, 95:231101, Dec 2005.
- [155] M. G. Linton. Reconnection of nonidentical flux tubes. *Journal of Geophysical Research: Space Physics*, 111(A12), 2006. A12S09.